

A STUDY OF TIP CLEARANCE MODEL EFFECTS ON COMPUTATIONAL
SIMULATION COSTS FOR NASA ROTOR 37

By

Parthasarathy Rajarathinam Jayachandran, B.Eng

Aeronautical Engineering

Anna University, Chennai, India, 2010

A thesis presented to Ryerson University

In partial fulfillment of the requirements for the degree of

Master of Applied Science in the Program of

Aerospace Engineering

Toronto, Ontario, Canada,

© Parthasarathy Rajarathinam Jayachandran, 2014

I hereby declare that I am the sole author of this thesis. This is a true copy of the thesis, including any required final revisions, as accepted by my examiners.

I authorize Ryerson University to lend this thesis to other institutions or individuals for the purpose of scholarly research.

I further authorize Ryerson University to reproduce this thesis by photocopying or by other means, in total or in part, at the request of other institutions or individuals for the purpose of scholarly research.

I understand that my thesis may be made electronically available to the public.

Acknowledgement

First and foremost, I would like to express my deepest gratitude to my supervisor, Dr. Jason V. Lassaline for his patience, motivation, immense knowledge and enthusiasm. Without his continuous encouragement and support, this thesis would not have been completed or written.

I would like to thank my friends for helping me achieve my goals and for their moral support.

Finally, I thank my parents Jayachandran and Shanthi, for their unconditional support and faith in me.

Abstract

The computational time and resources required to calculate an accurate solution is the key concern in the field of CFD. Especially in the CFD analysis of turbomachines many simulations are required to validate the CFD code and to predict the performance of the turbomachines. In this thesis, the typical computational domain was remodelled and the best computational settings were identified to compute the flows. By modifying the numerical domain, improved grid distribution with less number of nodes was achieved and the results predicted were within the limits specified by NASA for the validation of CFD codes. The modified model with the best computational settings required 28.3% less computational time and 20.5% less computer memory than the typical model and baseline methods.

TABLE OF CONTENTS

Acknowledgement	iii
Abstract	iv
LIST OF FIGURES	viii
LIST OF TABLES	xii
NOMENCLATURE	xiii
1. INTRODUCTION	1
1.1 Turbomachinery	1
1.1.2 Transonic Compressor Rotor	4
1.2 CFD & Challenges Associated with Numerical Simulations	7
2. REVIEW OF TURBOMACHINERY CFD	10
2.1 Introduction.....	10
2.2 Governing Equations for a Rotating System	10
2.3 Computational Grid	11
2.3.1 Structured Mesh	12
2.3.2 Unstructured Mesh.....	14
2.3.3 Hybrid Mesh	15

2.4	Turbulence Modelling.....	15
2.4.1	One-Equation Spalart-Allmaras Model	16
2.4.2	Two Equation Turbulence Models.....	18
2.4.3	Validation of Turbulence Models.....	20
2.5	Code Validation	22
3.	THE TEST CASE	25
3.1	NASA Rotor 37	25
4.	METHODOLOGY AND RESULTS	32
4.1	Numerical modelling	32
4.1.2	Effect of Grid density.....	38
4.2	Performance assessment	44
4.2.1	Computational Performance of Model-I B and Model- II B	44
4.2.2	Performance of Model-III.....	55
4.2.3	Block-Interface Effects	60
4.2.4	Inlet and Outlet Effects	63
4.2.5	Conclusion on Performance assessment.....	63
4.3	Computational Resources assessment.....	63

4.4	Discussions	64
4.4.1	Performance vs. Computational Resources	64
4.4.2	Effects of Geometrical Remodelling	65
5	CONCLUSIONS & RECOMMENDATIONS.....	66
	REFERENCES.....	68

LIST OF FIGURES

Figure 1 GP7200 Jet fan engine [4].	2
Figure 2 Shock configuration in a transonic compressor [6]	4
Figure 3 Shock propagation at different operating conditions [6]	5
Figure 4 Perspective views of shock in a transonic rotor. [7]	6
Figure 5 H-Grid [23]	13
Figure 6 C-Grid [24]	13
Figure 7 O-Grid [25]	13
Figure 8 Blade and flow path coordinates [20]	27
Figure 9 Measurement stations [20]	28
Figure 10 Overall performance at station 4 [20]	29
Figure 11 MODEL-I (Complete Blade)	33
Figure 12 MODEL-II	34
Figure 13 MODEL-III	34
Figure 14 Model-I with Boundary conditions	37
Figure 15 Model-II with Boundary conditions	37
Figure 16 Total pressure ratio Vs. Normalized mass flow rate for Model-I A, B, and C	39

Figure 17 Adiabatic efficiency Vs. Normalized mass flow rate for MODEL-I A, B, and C	39
Figure 18 Total pressure ratio Vs. Normalized mass flow rate for MODEL-II A, B and C	40
Figure 19 Adiabatic efficiency Vs. Normalized mass flow rate for MODEL-II A, B and C	40
Figure 20 Model-I B grid distribution on the hub.....	42
Figure 21 Model-I B grid distribution along the blade and hub	42
Figure 22 Model-II B grid distribution on the hub	43
Figure 23 Model-II B grid distribution along the blade and hub	43
Figure 24 Detailed view of computational domain Model-II B	46
Figure 25 Block interfaces in Model-II B.....	46
Figure 26 Periodic condition - rotational periodicity (Model-II B).....	47
Figure 27 Closer view of the tip-face (Model-II B).....	47
Figure 28 Total pressure ratio Vs. Normalized mass flow rate (Model-I B and Model-II B)	48
Figure 29 Total temperature ratio Vs. Normalized mass flow rate (Model-I B and Model-II B)	48
Figure 30 Adiabatic efficiency Vs. Normalized mass flow rate (Model-I B and Model-II B).....	48
Figure 31 Total pressure ratio along span at station 4 (Model-I B).....	49
Figure 32 Total pressure ratio along span at station 4 (Model-II B)	49
Figure 33 Total temperature ratio along span at station 4 (Model-I B).....	50

Figure 34 Temperature ratio along span at station 4 (Model-II B).....	50
Figure 35 Total pressure ratio along span comparison between Model-I B and II B.....	51
Figure 36 Total temperature ratio along span comparison between Model-I B and II B	51
Figure 37 Comparison of computational grid between Model-II B and other models.....	53
Figure 38 Blade-Blade Mach number contour at 70% span and 98% choked flow for experimental data [61]	54
Figure 39 Blade-Blade Mach number contour at 70% span and 98% choked flow (Model-IB)..	54
Figure 40 Blade-Blade Mach number contour at 70% span and 98% choked flow (Model-II B)	54
Figure 41 Computational domain of Model-III (No face tip).....	56
Figure 42 Periodic Boundary condition (Model-III)	57
Figure 43 Total pressure ratio Vs. Normalized mass flow rate (Model-I B, II B and III).....	57
Figure 44 Total temperature ratio Vs. Normalized mass flow rate (Model-I B, II B and III)	58
Figure 45 Adiabatic efficiency Vs. Normalized mass flow rate (Model-I B, II B and III)	58
Figure 46 Blade-Blade Mach number contour at 70% span and 98% choked flow (MODEL-III)	59
Figure 47 Tip Vortex flow	60
Figure 48 Mach number distribution at Station 2 and span 50% at 98% choked flow.....	62

Figure 49 Mach number distribution at Station 3 and span 50% at 98% choked flow..... 62

LIST OF TABLES

Table 1 Aerodynamic survey measurement locations and flow conditions at Station 1 [20].....	31
Table 2 Models description (Model-I, Model-II, Model-II)	33
Table 3 Models with multidomain structured grid	35
Table 4 Sub-models for grid density study	38
Table 5 Grid construction	41
Table 6 Computational Results of Model-III.....	56
Table 7 Computational model description (Model-II D, E, F, G)	61
Table 8 Computational Resources Assessment	64

NOMENCLATURE

Ω :	speed of rotation
\vec{V} :	Absolute velocity
\vec{W} :	Relative velocity
\vec{U} :	Whirl velocity
\vec{r} :	Radius
\vec{q}_t :	Turbulent heat flux
H_R :	Rothalpy
D:	Damping function
$\bar{\sigma}$:	Stress tensor
ρ :	Density,
p :	Pressure
$\bar{\tau}$:	Viscous stress
\vec{F} :	Body force
S_h :	Source term
H:	Enthalpy
\bar{D} :	Mean rate of strain tensor
\bar{I} :	Kronecker tensor
k :	Thermal conductivity

P_s :	Static pressure
E_R :	Relative internal energy
T_{ref} :	Sea level standard atmosphere
T_{t1} :	Inlet total temperature
$\bar{\tau}_t$:	Reynolds stress
K :	Turbulent kinetic energy
μ_t :	Viscosity
S :	Vorticity
$\tilde{\nu}$:	Eddy viscosity
ν_t :	Turbulent kinematic viscosity
d_t :	Distance between the local point and the transition point
U_τ :	Friction velocity
Δx_t :	Grid spacing along the wall at the nominated transition point
w_t :	Vorticity at the wall at the nominated transition point
Re_t :	Turbulent Reynolds number
k_R^+ :	Non-dimensional surface roughness
N :	Equivalent rotational speed
P_{ref} :	Sea level standard atmosphere
P_{t1} :	Inlet pressure
\dot{m} :	Mass flow rate

\dot{m}_{choke} : Choked mass flow rate

A_{an} : Annulus area

P_{04}/P_{01} : Total pressure ratio

η : Adiabatic efficiency

1. INTRODUCTION

1.1 Turbomachinery

Turbomachines are machines that transfer energy between a rotating component and the fluid flowing through them. Turbomachinery is broadly used in industries, agriculture, and daily life as propellers, compressors, gas or steam turbines, wind turbines and also as fans for cooling microprocessors. A general definition of turbomachinery given by Gorla [1] states, “Turbomachinery is a device in which energy transfer occurs between a flowing fluid and a rotating element due to dynamic action, and results in a change in pressure and momentum of the fluid”. The rotating component is called a rotor, which consists of one or several rows of rotating blades and typically there also exists a stator that has one or several rows of stationary blades. Each set of rotor and stator is called a stage.

Turbomachines are generally classified under two categories based on the energy transfer between the components and moving fluid. In the first category the work is done on the fluid i.e. the energy is transferred to the fluid, consuming power and increasing the total pressure of the fluid. Compressors, fans, and pumps all fall under the first category. In the second category the work is done by the fluid i.e. the energy is transferred from the fluid to the rotor, generating power. Gas turbines, steam turbines and hydraulic turbines fall under the second category. Based upon the inlet and outlet flow of the fluid the turbomachines can be classified as either axial turbomachinery or radial turbomachinery [2]. It was recorded that a primitive turbomachine called a waterwheel was invented more than hundred years ago to produce power [3]. Although the construction was simple, it followed the same basic principle with other complicated modern turbomachines such as the compressor and the gas turbine in a jet engine. A jet engine is

typically composed of a compressor, a combustion chamber and a gas turbine. For example, the GP7200 engine designed by Engine Alliance for the Airbus 380 is shown in Figure 1. In any jet engine, air is compressed by the compressor to increase density, while reducing the air velocity before entering the combustion chamber. The compressed air is mixed with the aviation fuel and burnt to produce a hot gas. Then the hot gas, which is at a high pressure and temperature, is expanded to extract energy as it passes through the turbines and further expanded in the nozzle to accelerate the flow.

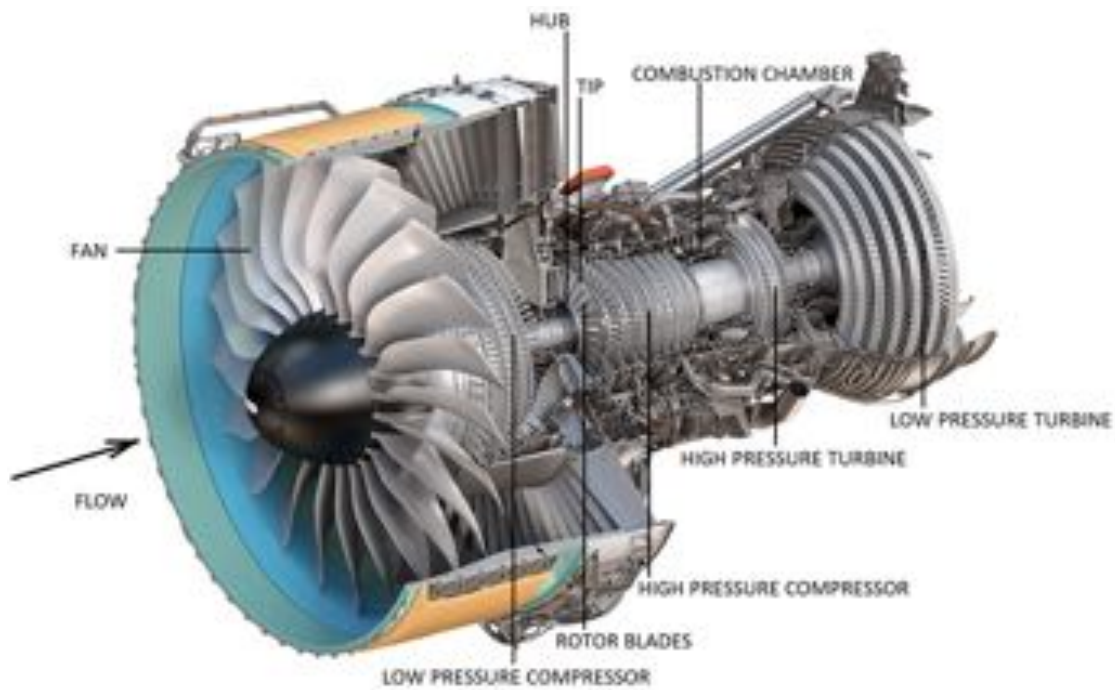


Figure 1 GP7200 Jet fan engine [4].

From the beginning of jet engine development in the late 1930s until now, turbojet engines require compressors and turbines with high-pressure ratios to gain higher efficiencies. In the late 1980s, many research organizations and manufacturers had launched series of research projects to develop advanced compressors and turbines, such as Integrated High Performance Turbine Engine Technology (IHPTET) and the Versatile Affordable Advanced Turbine Engines

(VAATE). Engine performance is typically evaluated in terms of the thrust-to-weight ratio (TWR) and the fuel consumption rate. Performance can be improved via a well-designed compressor and turbine with less stages and higher efficiency. Therefore, major researching efforts have been invested on improving the performance of compressor and turbine stages. On the industrial side, steam turbines and gas turbines are the main tool of power generation, where higher efficiency is equally important. At present, the modern compressor stage has a polytropic efficiency of about 90% and the modern turbine stage has a polytropic efficiency of up to 95% [3]. Further improvements need deeper understanding of the flow field inside the turbomachinery, which can be very difficult and challenging to study experimentally.

The turbomachinery design is a difficult task due to the complicated flow phenomenon, which involves interaction of various fields such as aerodynamics, thermodynamics, structural dynamics and high temperature materials. Among these, aerodynamic analysis is the center of the design, which ultimately decides the performance of turbomachinery. These flows are strongly 3D with significant viscous effects, and may be laminar, turbulent and transitional, including wake flow and secondary flows. It is possible for other complex flow phenomena to occur, such as transition, boundary layer separation, shock and shock-boundary layer interaction, unsteady interactions between the blade rows, and interactions between the blade row and end-wall [5]. Without numerical analysis such as Computational Fluid Dynamics (CFD) analysis, it is impractical to meet the growing rigorous needs of turbomachinery design. Hence, the study on numerical analysis and numerical design of turbomachinery are extremely essential. A NASA report “Numerical Simulation of Complex Turbomachinery Flows” [3] written in 1999, states that the complex flows in turbomachinery will remain the key research problems of

turbomachinery for the next few decades. The types of flows identified as being of the most interest are:

- Unsteady flow.
- Transition flow.
- Three-dimensional flows in tip leakage effect and film cooling.

The investigation in the present thesis will discuss the best numerical method and computational parameters to be selected to computationally model the turbomachinery flows with the least computational resources, with regards to flow about the tip of the blade. A detailed literature review and discussion of existing methods and procedures are presented in Chapter 2. This thesis focuses only on the axial turbomachinery, in particular the tip region of a transonic compressor rotor. The concepts related to transonic compressor rotors are presented in the following section.

1.1.2 Transonic Compressor Rotor

The compressor unit of an aircraft engine typically covers 50%-60% of the engine length and accounts for 40%-50% of the total weight [4]. Compressor stages must provide higher values of both polytropic efficiency and total pressure ratio to improve the performance of the engine. A higher value of total pressure ratio results in a decrease in the number of stages and, consequently, reduces the compressor weight and size.

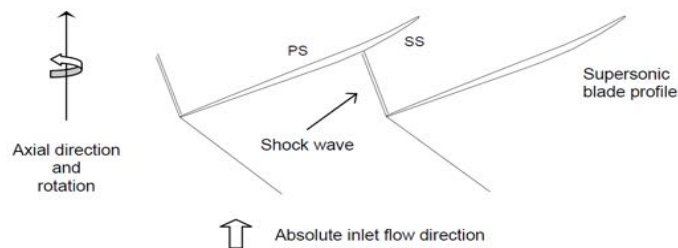


Figure 2 Shock configuration in a transonic compressor [6]

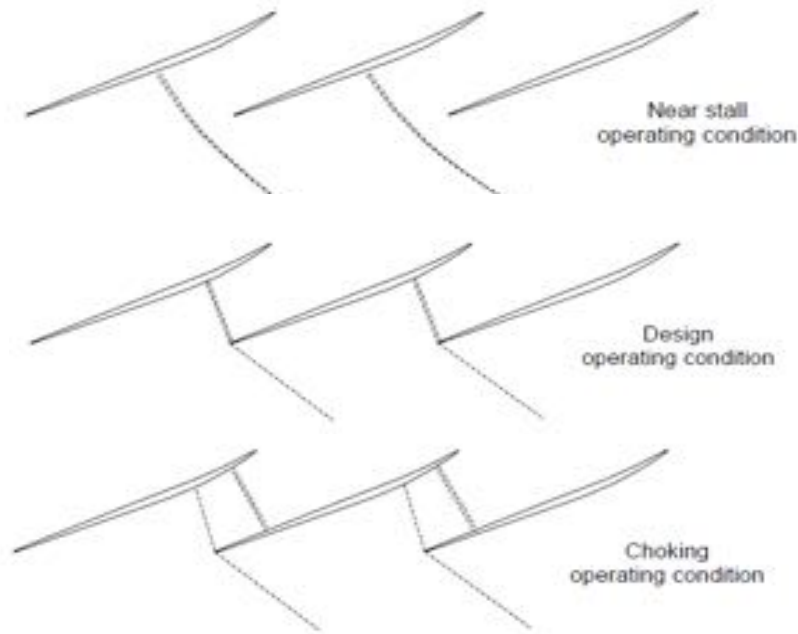


Figure 3 Shock propagation at different operating conditions [6]

The current method to achieve a higher total pressure ratio per stage is to increase the rotor tip speed. This increases the relative flow velocities at the outer span, leading to a transonic flow field that is supersonic at the outer span and subsonic at the lower span. The deflection forced by the pressure-side of the blade on the supersonic relative flow creates the shock wave, which begins from the blade leading edge and spreads into the blade passage (see Figure 2) [6]. As a result, transonic compressor rotors lack efficiency and operating range in comparison to traditional subsonic rotors due to the existence of strong shock waves.

Shocks are an irreversible process and increases entropy of the flow, which in turn reduces the overall rotor efficiency. Further, the interaction of secondary flows with the shock, such as a tip clearance flow, have a negative impact on the overall performance of the rotor. The shock-tip clearance flow interaction is can trigger stall in transonic compressor rotors.

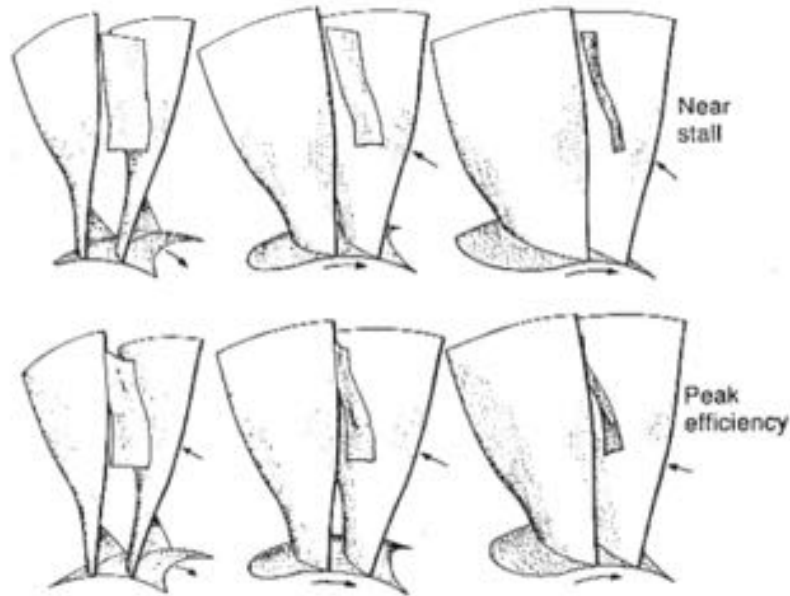


Figure 4 Perspective views of shock in a transonic rotor. [7]

The shock may also develop in different ways depending on the rotor geometry and operating conditions. Figure 3 shows the blade-to-blade shock development inside a basic transonic compressor rotor, varying from the choked flow condition to a near stall condition under constant wheel speed [6]. In general, the shock moves upstream and is positioned normal to the arriving flow due to the higher flow incidence at low mass flow rate conditions. This can be observed in the Figure 4, which illustrates three-dimensional views of shocks at both peak efficiency and near stall conditions in a basic transonic rotor [7].

The complexity of the flow field makes it very difficult for the numerical modelling and aerodynamic optimizations of transonic compressor rotors. In the last fifteen years many theoretical, experimental and CFD analyses were carried out to better understand the aerodynamic performance of these rotors. But research efforts are still needed to address the complex flow features that are not still completely understood and, as a result, the optimization process remains tough.

1.2 CFD & Challenges Associated with Numerical Simulations

Numerical simulations are used for the researches as an important support tool to experiments due to the complexity of the three dimensional internal flow in turbomachinery. Generally experiments can be costly and time consuming, even difficult to carry out at some specific conditions, for example very high altitude performance test. Computational Fluid Dynamics, is described by Hirsch [8] as "the set of methodologies that enable the computer to provide us with a numerical simulation of fluid flows". A fluid flow field can be modelled by approximating a solution to the set of Partial Differential Equations (PDE) known as the Navier-Stokes (NS) equations. These PDEs are highly nonlinear such that the analytical solutions are currently possible only for limited simple cases. CFD simulates the solution to the governing PDE using numerical methods. The general steps to complete a CFD analysis include spatial discretization (pre-processing) of the problem, time integration including turbulent flow approximation (solver), followed by flow visualization (post-processing). For complex cases additional methods are required, for instance the treatment of rotor-stator interaction in the case of turbomachinery.

Computational engineering has grown into a main pillar of engineering research, supporting analytical/theoretical and physical/experimental research. With the developments and propagation of computational tools and methodology, the applications of CFD have grown to include problems of larger magnitude and complexity. Turbomachinery simulations have many challenges and complexities to be resolved, such as meshing complex three-dimensional geometries, determining relative mesh motion among moving components, compressibility effects, transonic flows, resolving shocks, and most importantly modeling turbulence. [9]

Numerous numerical methods for simulating rotating machinery were developed and published over the past few decades. This period of development began with the development by Ni [10] of multiple-grid schemes for solving the Euler equations, and the time-marching analysis of steady transonic flow through turbomachinery cascades by Delaney [11]. Adamczyk ([12], [13]) detailed numerical aspects of unsteady flow calculations and models for multistage turbomachinery flow simulations. Hah ([14], [15]) in 1984 demonstrated simulations of the Navier-Stokes for flow through turbines and compressor rotors. Weinberg et al. [16] further developed analysis of three-dimensional viscous, transonic flow and Chima et al. [17] followed with major advancements in the simulation of the three-dimensional viscous flows associated with turbomachinery. The analytical algorithms used for predicting performance of rotating machinery prior to these endeavours were largely based on empiricism ([14], [18]).

The focus of this research is to reduce the computational resource requirements for simulating flow through turbomachinery, and to study the role of computational domain complexity and solver settings in management of the computational costs. The parameters affecting the accuracy were studied through a literature review conducted on the research works applied to turbomachinery flows. For reducing the computational resources (computational time and memory) while maintaining the prediction accuracy the following aspects were considered: modelling of the geometry, partitioning of the domain, redistribution of the grid elements, determining the effects of tip clearance, interface methods and boundary conditions. The modifications made to the flow domain of Rotor 37 reduced the complexities in the geometry and this resulted in a better distribution of grid elements with less number of nodes. Additionally, best computational settings (boundary conditions and interface methods) were identified for the

modified domain. All of these efforts contributed to a unique method that required 28.3% less computational time and 20.5% less computer memory than the traditional methods.

The studies and techniques followed are categorized under the following chapters. Chapter 2 discusses how the governing equations are modified for a rotating system, the different types of grids in use, and the mesh strategies for use near the blade walls and far fields. It also presents the state-of-the-art of numerical methods used for solving the compressible Navier-Stokes equations in turbomachinery applications and summarizes the methods to reduce the computational resources while retaining the prediction accuracy. Chapter 3 gives an overview of the NASA test case Rotor 37. The geometry specifications, details of the experimental setup and experimental measurements are provided in this chapter. Chapter 4 presents i) the different models created for this research and the respective modelling methods ii) a grid density study iii) an assessment on the predictions by the models iv) an assessment on the computational resources required by the models for accurate prediction, and v) a comparison between model predictions based upon computational requirements. Finally, Chapter 5 concludes the research with the benefits of domain remodelling and best computational settings.

2. REVIEW OF TURBOMACHINERY CFD

2.1 Introduction

The development of numerical methods and computational facilities has extended to the use of Computational Fluid Dynamics as a tool for designing and analysing many components of gas-turbine engines. It is possible to predict many of the flow properties and the losses due to shocks, viscous layers, tip clearance effects, and passage vortices. This chapter is a short presentation of the state-of-the-art of numerical methods used for solving compressible Navier-Stokes equations in turbomachinery applications.

2.2 Governing Equations for a Rotating System

This section is about the formulation of the Reynolds Averaged Navier-Stokes (RANS) equations applied to turbomachinery flow calculations, for the full 3D system written in a rotating frame of reference. It is required to describe the flow behaviour relative to a rotating frame of reference that is attached to the rotor. To formulate the equations in a rotating frame of reference consider a point in turbomachinery that is rotating with a steady speed of rotation $\vec{\Omega}$. By using the relative time derivative definitions, and by recalling that the absolute velocity \vec{V} and the relative velocity \vec{W} are related by [19]

$$\vec{V} = \vec{W} + \vec{U}. \quad (1)$$

Where whirl velocity $\vec{U} = \vec{\Omega} \times \vec{r}$, and \vec{r} being the location of \vec{V} relative to the origin of rotating frame.

In a first approach the governing equations for mass, momentum, and energy are written by using the relative velocity

$$\frac{\partial \rho}{\partial t} + \nabla \cdot \rho \vec{W} = 0, \quad (2)$$

$$\frac{\partial}{\partial t}(\rho \vec{W}) + \nabla \cdot (\rho \vec{W} \vec{W}) + \rho(2\vec{\Omega} \times \vec{W} + \vec{\Omega} \times \vec{\Omega} \times \vec{r}) = -\nabla p + \nabla \bar{\tau}_r + \vec{F}, \quad (3)$$

$$\frac{\partial}{\partial t}(\rho E_r) + \nabla \cdot (\rho \vec{W} H_r) = \nabla \cdot (k \nabla T + \bar{\tau}_r \cdot \vec{W}) + S_h. \quad (4)$$

Where $2\vec{\Omega} \times \vec{W}$ is the Coriolis acceleration, $\vec{\Omega} \times \vec{\Omega} \times \vec{r}$ is the centripetal acceleration, $\bar{\tau}_r$ is the viscous stress calculated using relative velocity, E_r is the relative internal energy, ρ is the density, p is the pressure, \vec{F} is the body force, k is the thermal conductivity, S_h is the source term and H_r is the relative total enthalpy also known as the rothalpy. [19]

The second approach is to write the governing equations by using the absolute velocity

$$\frac{\partial \rho}{\partial t} + \nabla \cdot \rho \vec{W} = 0, \quad (5)$$

$$\frac{\partial}{\partial t} \rho \vec{V} + \nabla \cdot (\rho \vec{W} \vec{V}) + \rho(\vec{\Omega} \times \vec{V}) = -\nabla p + \nabla \bar{\tau} + \vec{F}, \quad (6)$$

$$\frac{\partial}{\partial t}(\rho E) + \nabla \cdot (\rho \vec{W} H + \rho \vec{U}) = \nabla \cdot (k \nabla T + \bar{\tau} \cdot \vec{V}) + S_h. \quad (7)$$

In this formulation, the Coriolis and centripetal accelerations can be collapsed into a single term $\vec{\Omega} \times \vec{V}$. The relative velocity formulation is preferred in analysis where most of the fluid in the domain is rotating and absolute velocity is preferred when most of the fluid is not rotating [19]. In the current thesis, the entire computational domain is set to be rotating with the fluid, therefore the relative velocity formulation is used.

2.3 Computational Grid

One of the essential requirements to obtain reliable numerical solutions for turbomachinery flow analysis is the generation of the computational mesh. The generated mesh should deal with various complex geometries and conditions such as axial or centrifugal machines, rotor-stator interaction, tip clearance, and highly cambered blades. Since the beginning of three-dimensional CFD simulations there have been large improvements in mesh generation techniques. Numerous

meshing methods and types have been proposed over the last decade from simple C-grids to complex hybrid multi-domain meshes. Traditionally, 3D meshes have been constructed by stacking two-dimensional blade to blade meshes. Further due to complicated geometries and advanced turbulence models, an increasing number of mesh techniques take into account adaptive refinement where mesh elements are automatically refined based upon an estimate of the ϵ error. The developments in this area shows an increasing number of mesh strategies, conforming to different intensities of mesh generation, and also to different methods of numerical domain modelling in terms of computational resources management. By taking into account some typical examples, a review of the most important mesh generation techniques are presented in the following sections. [20]

2.3.1 Structured Mesh

Three types of grids can be considered for a mono-domain (made up of one type of grid) structured methodology: the H-grid, C-grid and O-grid methods. An H-grid (see Figure 5) is appropriate for far-field and periodicity conditions, and is typically simple to create. However the elements of an H-grid often become highly skewed near sharp edges, in particular close to the leading and trailing edges of a blade. To avoid high skewness a C-grid (see Figure 6) is often generated around the perimeter of the blade and in the wake region to provide good resolutions. Unfortunately, a C-grid is often skewed at the inlet and periodic conditions. While an O-grid (see Figure 7) can provide good resolution at both leading and trailing edges, it too can become highly skewed at inflow, outflow and periodic boundary faces. [20]

Veullot [21] and Arnone [22] in 1993 demonstrated the use of non-periodic meshes to counter these problems at the periodic boundaries. A more common method today is the structured multi-

domain technique, which retains the advantages and eliminates the disadvantages of the single domain grids.

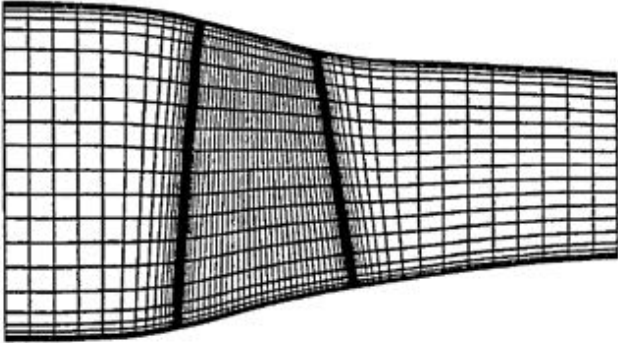


Figure 5 H-Grid [23]

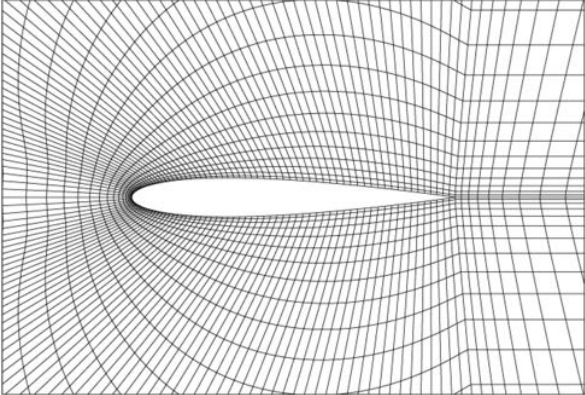


Figure 6 C-Grid [24]

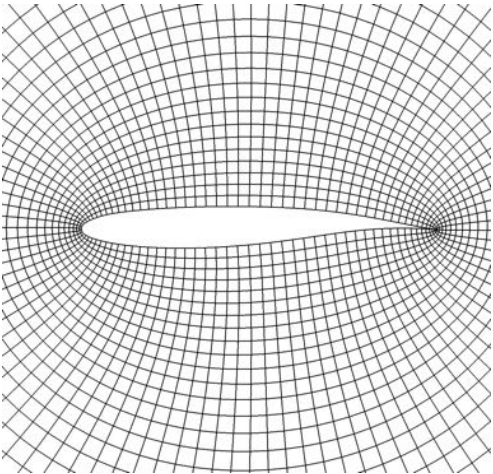


Figure 7 O-Grid [25]

To avoid inaccuracies and simulation problems, multi-domain grids (a computational domain made up of more than one type of grid) should be very smooth at the interfaces of two different grid blocks. Heider [26] used a five-domain mesh to model an extremely cambered turbine with a tip clearance gap. The five-domain method provided a good quality of mesh in all the domains with an H-O decomposition at the tip clearance to provide a high-quality grid with regular spacing in the radial direction. Fougères [27] and Choi [28] showed that a good discretization of the viscous layer and capture of flow interaction was possible by multi-domain mesh method using overlapping meshes. Kim et al [29] utilized H/J/C/L grid topology with dimensionless wall distance $y^+ \leq 2$ to produce a better quality mesh for asymmetric aerofoil blades and to accurately capture the wall shear stress.

Yin et al [30] created the contour line of the wall distance first to satisfy the boundary layer requirement of the distance of the first point from the wall for the turbulence model. The grid used in the solver was a simple H mesh formed from stacking two-dimensional grids along the span. For the simulation of efficiency enhancements in transonic compressor rotor, Benini et al [31] used a multi-block structured grid. In this case, an H-type topology was selected for both the inlet and outlet blocks, and a composite J/O-type grid was selected to fit the passage block. The grids had a very low level of skewness and were adequately resolved at the near-wall regions, as required for an accurate simulation of the boundary layer near the blades.

2.3.2 Unstructured Mesh

The unstructured tetrahedral mesh method leads to a higher flexibility in the mesh generation process in comparison to the structured mesh method. Bassi [32] and Trepanier [33] used the unstructured mesh method to solve for the two-dimensional flows in a blade cascade and three-

dimensional flows in a rotor/stator interaction study. Kwon [34] adapted a similar mesh technique to solve Euler calculations on turbine blades. In all these researches, it was difficult to provide adequate resolution of the boundary layer region and wake regions. But, Dawes [35] was able to capture a very accurate shock/boundary layer interaction by adaptive mesh refinement. Adequate grid resolution is possible by producing meshes with fine spacing normal to the flow direction, and a coarser spacing in the direction of the flow. The result is a mesh with high-aspect elements which typically cause convergence issues (numerical stiffness) for most solvers. Thus far unstructured solvers are less efficient in CPU time than structured solvers [36].

2.3.3 Hybrid Mesh

The hybrid method is the combination of structured and unstructured meshes. This method makes use of the advantages of both the approaches. Nakahashi et al [37] and Mathur et al [38] used the hybrid mesh method to solve the Navier-Stokes equations for a turbine cascade simulations and for rotor-stator interactions. Both authors created an orthogonal, structured mesh in the vicinity of the blades (overlapping the predicted location of the boundary layer) and an unstructured mesh further away. This contributed to a mesh with an overall higher quality, particularly in the far fields and close to the periodic boundaries.

2.4 Turbulence Modelling

The RANS model formulated with the system of equations (3) and (4) needs to be closed for solving purposes; therefore it is necessary to model the Reynolds stress $\bar{\tau}_t$, and the turbulent heat flux \bar{q}_t . There are two classes of turbulence model, utilized at the engineering level. The first one, corresponding to the majority of turbulence models used, is defined by the eddy-viscosity concept. The eddy-viscosity concept, also called the Boussinesq hypothesis, in which the

turbulent stress tensor $\bar{\tau}_t$ and the turbulent heat flux \bar{q}_t are expressed by relations similar to those existing for the laminar tensor and heat flux, can be written as

$$\bar{\tau}_t = -\frac{2}{3}(\rho k + \mu_t \vec{\nabla} \cdot \vec{\nabla})\bar{I} + 2\mu_t \bar{D}, \quad (8)$$

$$\bar{q}_t = -C_p \mu_t / Pr_t \vec{\nabla} T. \quad (9)$$

Where Pr_t is the Prandtl turbulent number, \bar{D} is the mean rate of strain tensor, \bar{I} is the Kronecker tensor and C_p is the specific heat at constant pressure. The modelling difficulty is thus reduced to the determination of two scalar quantities, the turbulent viscosity μ_t and the turbulent kinetic energy k . There are two distinct methods for the models adopting the Boussinesq hypothesis. The first method is composed of algebraic turbulence models, in which the eddy viscosity is determined from the characteristic properties of the boundary layer and the turbulent kinetic energy is considered to be zero, as it cannot be estimated. The second method is transport equation models, where the eddy viscosity is usually linked to the turbulent kinetic energy and to a characteristic length scale of turbulence, stated in terms of the local turbulent quantities. The second class of turbulence model does not adopt the Boussinesq hypothesis and is based on Reynolds Stress Models (RSM) and Algebraic Stress Models (ASM). The RSM models solve a transport equation for all the stresses and the ASM Models make use of two transport equations that are closed by algebraic relations for the Reynolds stresses. [20]

2.4.1 One-Equation Spalart-Allmaras Model

There had been major interest in one-equation transport models as a method to retain the advantages of a transport model at a minimum computational cost. Perhaps the most accepted one equation model is the Spalart-Allmaras model [39, 40] that solves an equation for the high Reynolds number eddy viscosity $\tilde{\nu}$ written in the following form

$$\frac{D\tilde{v}}{Dt} = C_{b1}[1 - f_{t2}]\tilde{S}\tilde{v} + \frac{1}{\sigma}[\nabla \cdot ((v + \tilde{v})\nabla\tilde{v}) + C_{b2}(\nabla\tilde{v})^2] - \left[C_{w1}f_w - \frac{C_{b1}}{K^2}f_{t2}\right]\left[\frac{\tilde{v}}{d}\right]^2 + f_{t1}\Delta U^2. \quad (10)$$

The turbulent kinematic viscosity, ν_t , is given by

$$\nu_t = \tilde{v}.f_{v1}, \quad (11)$$

$$\text{where } f_{v1} = \frac{\chi^3}{\chi^3 + C_{v1}^3} \text{ with } \chi = \frac{\tilde{v}}{v}, \quad (12)$$

$$\tilde{S} = S + \frac{\tilde{v}}{K^2 d^2} f_{v2}, \quad (13)$$

where S is the vorticity,

$$f_{v2} = 1 - \frac{\chi}{1 + \chi f_{v1}}, \quad (14)$$

$$f_w = g \left[\frac{1 + C_{w3}^6}{g^6 + C_{w3}^6} \right], g = r + C_{w2}(r^6 - r), r = \frac{\tilde{v}}{\tilde{S}K^2 d^2} \quad (15)$$

$$f_{t2} = C_{t3} \exp(-C_{14}\chi^2), \quad (16)$$

$$f_{t1} = C_{t1}g_t \exp\left(-C_{t2} \frac{w_t^2}{\Delta U^2} [d^2 + g_t^2 d_t^2]\right), \quad (17)$$

$$g_t = \min(0.1, \Delta U/w_t \Delta x_t), \quad (18)$$

where:

Δx_t is the grid spacing along the wall at the nominated transition point

d_t is the distance between the local point and the transition point

w_t is the vorticity at the wall at the nominated transition point

The values of constants used are typically

$$C_{b1} = 0.1355, \sigma = 2/3, C_{b2} = 0.622, K = 0.41, \quad (19)$$

$$C_{w1} = \frac{C_{b1}}{K} + \frac{1+C_{b2}}{\sigma}, C_{w2} = 0.3, C_{w3} = 2, \quad (20)$$

$$C_{v1} = 7.1, C_{t1} = 1, C_{t2} = 2, C_{t3} = 1.1, C_{14} = 2. \quad (21)$$

The boundary condition at the wall is imposed by setting $\tilde{v} = 0$.

2.4.2 Two Equation Turbulence Models

The two-equation turbulence models provide an excellent concession between accuracy and computational cost. The use of two transport equations for solving turbomachinery applications has been growing in the recent years [20]. Best examples of the two-equation turbulence models are Jones-Launder $k - \varepsilon$ model [41], Wilcox $k - \omega$ model [42], Wilcox-Rubesin $k - \omega^2$ model [43] and Coakley $q - \omega$ model [44]. The low Reynolds number $k - \varepsilon$ model and $k - \omega$ model, which are in fact the popular and most acceptable two-equation models, are discussed in this section. The advantage of these two models is that the low Reynolds number closure coefficients do not depend on geometrical quantities (i.e. the wall distance y^+) or on the friction velocity. Whereas based on the local flow quantities the damping functions solely depend on the turbulent Reynolds number, Re_t [20]

$$Re_t = \frac{\rho k^2}{\mu \varepsilon} = \frac{\rho k}{\mu \omega}. \quad (22)$$

The $k - \varepsilon$ model and $k - \omega$ model are as follows:

a) The equations of the $k - \varepsilon$ model is written as

$$\frac{\partial \rho k}{\partial t} + \vec{\nabla} \cdot (\rho k \vec{V}) = \vec{\nabla} \cdot \left[\left(\mu + \frac{\mu_t}{\alpha_k} \right) \vec{\nabla} k \right] + \bar{\tau}_t : \vec{\nabla} \vec{V} - \rho \varepsilon - D, \quad (23)$$

$$\frac{\partial \rho \varepsilon}{\partial t} + \vec{\nabla} \cdot (\rho \vec{V} \varepsilon) = \vec{\nabla} \cdot \left[\left(\mu + \frac{\mu_t}{\alpha_\varepsilon} \right) \vec{\nabla} \varepsilon \right] + C_1 f_1 \frac{\varepsilon}{k} \bar{\tau}_t : \vec{\nabla} \vec{V} - C_2 f_2 \frac{\varepsilon^2}{k} + E. \quad (24)$$

In these equations, D is a wall term and E is a low Reynolds term introduced to solve the $k - \varepsilon$ model in the region close to the wall with low turbulent Reynolds number ($Re_t \leq 100$).

The turbulent viscosity is evaluated by the relation $\mu_t = c_\mu f_\mu \rho k^2 / \mu \varepsilon$.

The Jones-Lauder $k - \varepsilon$ model is based on the following definitions:

$$D = 2\mu(\vec{\nabla}\sqrt{k})^2, E = 2\frac{\mu\mu_t}{\rho}\left(\frac{\partial^2 v_t}{\partial n^2}\right)^2, \quad (25)$$

$$\alpha_k = 1, \alpha_\varepsilon = 1.3, C_1 = 1.57, C_2 = 2, f_1 = 1, f_2 = [1 - 0.3\exp(-Re_t^2)], \quad (26)$$

$$f_\mu = \exp\left(\frac{-25}{1+Re_t/50}\right), C_\mu = 0.09. \quad (27)$$

The boundary conditions at the wall is imposed by setting $k = 0$ and $\varepsilon = 0$.

b) The equations of the $k - \omega$ model is written as

$$\frac{\partial \rho k}{\partial t} + \vec{\nabla} \cdot (\rho \vec{V} k) = \vec{\nabla} \cdot [(\mu + \sigma^* \mu_t) \vec{\nabla} k] + \bar{\tau}_t : \vec{\nabla} \vec{V} - \beta^* \rho k \omega, \quad (28)$$

$$\frac{\partial \rho \omega}{\partial t} + \vec{\nabla} \cdot (\rho \vec{V} \omega) = \vec{\nabla} \cdot [(\mu + \sigma \mu_t) \vec{\nabla} \omega] + \alpha \frac{\omega}{k} \bar{\tau}_t : \vec{\nabla} \vec{V} - \beta \rho \omega^2. \quad (29)$$

The turbulent viscosity is evaluated by the relation $\mu_t = \alpha^* \rho k / \omega$. The parameters

$\alpha, \alpha^*, \beta, \beta^*, \sigma, \sigma^*$ in the above equations are the closure coefficients of the model and are defined

by Wilcox [45] as:

$$\alpha = \alpha_t \frac{\alpha_0 + \frac{Re_t}{R\omega}}{1 + \frac{Re_t}{R\omega}} (\alpha^*)^{-1}, \quad \alpha^* = \alpha_t^* \frac{\alpha_0^* + \frac{Re_t}{Rk}}{1 + \frac{Re_t}{Rk}}, \quad (30)$$

$$\beta = \beta_t, \quad \beta^* = \beta_t^* \frac{\beta_0^* + (Re_t/R\beta)^4}{1 + (Re_t/R\beta)^4}, \quad (31)$$

$$\sigma = \sigma^* = \frac{1}{2}, \quad (32)$$

$$\alpha_0 = \frac{1}{10}, \quad \alpha_0^* = \frac{\beta_t}{3}, \quad \beta_0^* = \frac{5}{18}, \quad (33)$$

$$\alpha_t = \frac{5}{9}, \quad \alpha_t^* = 1, \quad \beta_t = \frac{3}{40}, \quad \beta_t^* = \frac{9}{100}, \quad (34)$$

$$R_\beta = 8, \quad R_k = 6, \quad R_\omega = 2.7. \quad (35)$$

At solid walls, $k = 0$ and $\omega = \frac{U_\tau^2}{\nu} S_R$ where the friction velocity $U_\tau = \sqrt{\frac{\tau_w}{\rho}}$. Parameter S_R is related to the non-dimensional surface roughness $k_R^+ = \frac{k_R U_\tau}{\nu}$ through the correlation

$$S_R = \left(\frac{50}{k_R^+}\right)^2 \text{ for } k_R^+ < 25, \quad (36)$$

$$S_R = \frac{100}{k_R^+} \text{ for } k_R^+ \geq 25, \quad (37)$$

where $k_R^+ \leq 5$ for smooth surfaces.

The $k - \omega$ model includes low Reynolds number modified closure coefficients, which are intended to simulate flow transitions. This form of the coefficients is not severely required in a turbulent boundary layer even if the equations are integrated very close to the wall [39].

2.4.3 Validation of Turbulence Models

The selection of the turbulence model for solving the RANS equations is very important to capture the core features of complex internal flows and to predict the losses. In this section several turbulence models with different levels of grid refinement used for solving turbomachinery flows are compared.

Chima et al [46] utilized a modified Baldwin-Lomax model to show that the results well matched with the experimental measurements of kinetic energy efficiency and heat transfer for a turbine cascade. Yi et al [47] performed numerical investigation on centrifugal compressor stages using the S-A turbulence model, the total pressure ratio was well predicted but the efficiency was underestimated by 1.5%. Beard et al [48] employed the one equation S-A turbulence model to analyze an un-shrouded transonic turbine, and accurately predicted the effects of tip leakage flow and casing secondary flows but demonstrated an under-prediction of the loss generated in the

turbine. This would be expected because of the simplified turbine geometry used in this CFD simulation. These researchers recommended the use of two-equation turbulence model or finer grids for more exact results.

A thorough study of the flow in a transonic fan was presented by Jennions and Turner [49] in 1993 using the Baldwin-Lomax and $k - \varepsilon$ models. In this paper, it is shown that an extended $k - \varepsilon$ model with multiple time scales, provides a better prediction of the shock position. Grönman et al [50] studied the performance of a supersonic axial turbine at off-design conditions by using the $k - \varepsilon$ turbulence model with a grid of $y^+ \leq 1$ next to the blade surface and frozen-rotor approach at the stator-rotor. The results showed that locations of the shocks were well predicted but the losses between the wake and suction surface were partly under predicted due to the weaker than measured shocks. Geng et al [51] computationally modelled a single rotor transonic compressor and presented that the $k - \varepsilon$ model gives a better demonstration of the shock behaviour but under predicts the separation zone. A 3D shock/boundary layer interaction in a transonic channel with a swept bump was measured and compared by Cahen [52]. The simulations were performed using the $k - \varepsilon$ model and the results showed that the prediction of shock/boundary layer interaction in the 2D cases were better than in the 3D corner regions. The $k - \varepsilon$ model predicts the separated regions even if the secondary flows were not perfectly reproduced. Yet, even if the key trends are well predicted, the $k - \varepsilon$ calculation does not accurately predict the level of kinetic energy and the length of the separation zone in the interaction region.

The tip clearance effects in a transonic compressor stage was investigated by Ciorciari et al [53] with a multi-block O-C-H topology for the computational grid and Wilcox $k - \omega$ turbulence

model. The turbulence model had several modifications to account for the effect of compressibility and rotation on the turbulence. The researchers presented that correct tip gap geometry is necessary to obtain an adequate prediction of the total pressure ratio. Also, a denser grid of 2.8 million number of nodes produced better results and converged approximately at 1000 iterations. Ernesto et al [31] enhanced the efficiency of the compressor rotor blades with the use of synthetic jets (zero mass flux and non-zero momentum flux), and showed that the $k - \omega$ SST turbulence model is well suited for flow fields dominated by adverse pressure gradients similar to the turbomachinery flow fields. At low flow operating condition, the shock front was well captured by the model and a quite good agreement between the calculated and measured Mach number values after the shock was observed. This is indicated by the fact that the blade boundary layer and its interaction with the shock were well calculated by the $k - \omega$ SST turbulence model.

2.5 Code Validation

As already pointed out, 3D steady viscous turbomachinery applications are generally computed at present with solvers which have been "calibrated" on typical test cases where comprehensive experimental data are accessible. To validate a solver, not only is the wall pressure distribution required but also other experimental measurements, like blade-blade Mach number contour, variation of relative Mach number along the pitch, temperature distribution and change in adiabatic efficiency with the mass flow rate [20]. In the current section, earlier and most recent researches are presented on compressor blade flow computations that are typical of the state of the art achieved for these configurations. Ahn and Kim [54] utilized a Baldwin-Lomax turbulence model with 0.64 million-node grid for the aerodynamic optimization of the compressor rotors, it took 3000 iterations and 23 hours for the solutions to converge.

Wet compression (or water injection in the compressor) performance of a transonic compressor rotor as analysed by Yang et al [55] with the $k - \varepsilon$ turbulence model and a rotor flow field with 0.5 million grid nodes. Calculations were started with 115534 Pa as outlet static pressure and the calculated flow rate was close to the measured maximum flow rate. The calculated efficiencies were lower than the experiment data by 2% to 3%.

Kim et al [29] evaluated the performance of a transonic axial compressor with H/J/C/L grid topology which provided better mesh quality for the asymmetric aerofoils, non-matching H-grid mesh at the tip clearance and used the SST turbulence model. The results showed that the adiabatic efficiency and pressure ratio were under predicted for 0.74 million number of grid nodes with $y^+ \leq 2$. Using an Intel Core I7 CPU 2.67GHz processor took approximately 7 hours as computational time and the researchers presented that the accuracy of the numerical scheme for turbulent flow is highly dependent upon treatment of the wall shear stress. The advantage of the SST model is that it uses a $k - \omega$ model at the near-wall region and $k - \varepsilon$ model in the bulk domain. Yin Song et al [30] numerically simulated an axial compressor with SST turbulence model and the flow region was modeled with a simple H mesh by stacking the 2-D stream face grid in the span wise direction. The computational results showed improvements in terms of overall performance and the distribution of the aerodynamic parameters. The SST model enhanced the quantitative predictions of the complex turbulent flows with strong adverse pressure gradients and separated flows encountered in axial compressors.

Based on the literature review the computational domains in this research are constructed as structured multi-domains and with grids that are very smooth at the interfaces. A denser grid is adopted with $y^+ \leq 1$ to produces better results, and to avoid high skewness H-grid is used at inlet and outlet blocks, with C-grids and O-grids around the perimeter of the blade. This gives

good resolutions in the grid distribution. As it is necessary to obtain an adequate prediction of the flow parameters in the radial direction the tip clearance are remodelled to provide with a high-quality grid that is regularly spaced in the radial direction.

Since the two-equation turbulence models provide an excellent concession between accuracy and computational cost, the $k - \varepsilon$ model and the SST model were compared for using in this research. From the literature review, the SST model is selected as the turbulence model in this research because it is well suited for turbomachinery flow fields and enhanced the quantitative predictions of the complex turbulent flows with strong adverse pressure gradients and separated flows encountered in axial compressors. Whereas, $k - \varepsilon$ model predicts the separated regions but does not accurately predicts the level of kinetic energy and the length of the flow. The main advantage of the SST model is that it uses a $k - \omega$ model at the near-wall region and $k - \varepsilon$ model in the bulk domain.

3. THE TEST CASE

The test case Rotor 37 selected in this thesis is a widely used reference test case by many researchers for the computational modelling of turbomachinery. It is an isolated axial-flow compressor rotor designed and studied experimentally at the National Aeronautics and Space Administration Lewis Research Center (US). The data sets were selected following a complete review of the experimental programmes and the available data. The test programmes were conducted in well-built test installations operated by experienced research groups. By these test programmes an extensive range of data were available, based on well-established instrumentation and data acquisition methods, and reduced by recognized and traceable procedures. As the Rotor 37 case had a large amount of proven experimental results it was selected as a suitable test case to validate CFD codes [20].

3.1 NASA Rotor 37

Rotor 37 was designed and originally tested by the NASA Lewis Research Center as part of a research involving four associated axial-flow compressor stages. These compressor stages were projected to cover a range of design constraints typical of aircraft gas-turbine engine high-pressure compressor stages.

In the case of stage 37, representative values were:

- Rotor inlet hub-to-tip diameter ratio 0.7
- Rotor blade aspect ratio 1.19
- Rotor tip relative inlet Mach number 1.48
- Rotor hub relative inlet Mach number 1.13
- Rotor tip solidity 1.29
- Blade airfoil sections Multiple-Circular-Arc (MCA)

No inlet guide vanes were introduced for any of the stages. Reid and Moore [56] were the first to report some design information and overall stage performance results, followed by more comprehensive stage performance result reported by Moore and Reid [57]. It is to be noted that while the designs and stage tests were instigated during the 1970's, geometries and performance levels were similar to those for current gas-turbine engine stages.

Design point values for the rotor as estimated in the design computations were:

Equivalent rotational speed:

$$N \sqrt{\frac{T_{ref}}{T_{t1}}} = 17188.7 \text{ rpm (1800 rad/s)}$$

Where T_{t1} = Inlet total temperature

$$T_{ref} = 288.15 \text{ K (Sea level standard atmosphere)}$$

Equivalent rotor tip speed:

$$U_t \sqrt{\frac{T_{ref}}{T_{t1}}} = 454.1 \text{ m/s}$$

$$\text{Equivalent mass flow per unit annular area } \frac{\dot{m}}{A_{an}} \frac{P_{ref}}{P_{t1}} \sqrt{\frac{T_{t1}}{T_{ref}}} = 200.5 \text{ kg/s/m}^2$$

Where P_{t1} = Inlet pressure

$$P_{ref} = 101.33 \text{ kN/m}^2 \text{ (Sea level standard atmosphere)}$$

$$A_{an} = \text{Annulus area}$$

$$\text{Rotor total pressure ratio} = 2.106$$

$$\text{Rotor polytropic efficiency} = 0.889$$

$$\text{Number of rotor blades} = 36$$

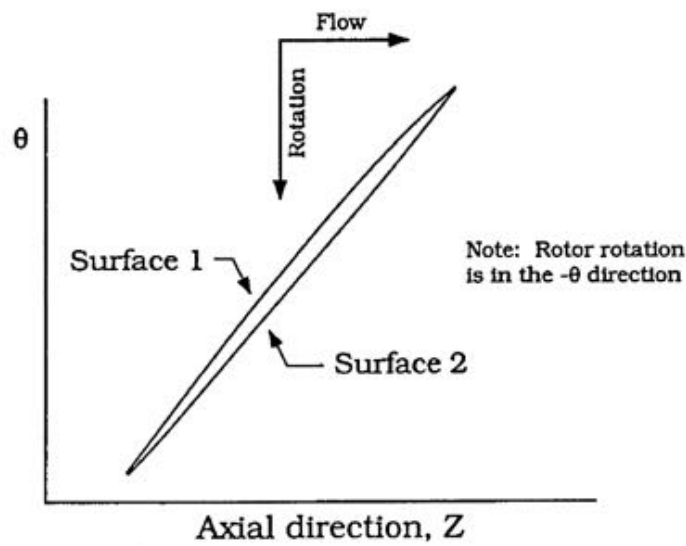
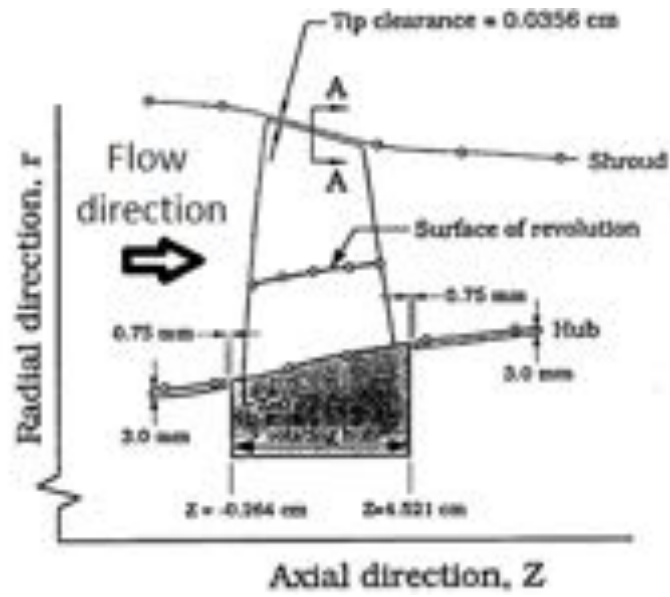


Figure 8 Blade and flow path coordinates [20]

Following the tests of Moore and Reid [57] on NASA Stage 37, the rotor was retested as an isolated component, recognized by NASA as Rotor 37. The Figure 8 illustrates the annular flow path and blade airfoil geometries with coordinate reference directions. These coordinate definitions are those used in all performance computations reported in other sections of this thesis. The data sets utilized in the AGARD and ASME code validation studies were measured

with NASA Rotor 37 operating at the design equivalent rotational speed 17188.7 rpm (1800 rad/s). To create the reference points for complete flow field measurements, overall performance was determined at equivalent mass flow rates from the maximum feasible referred as \dot{m}_{choke} , to a minimum, little more than the rotor stall flow. This near stall flow rate was experimentally determined to be $\dot{m}/\dot{m}_{choke} = 0.925$.

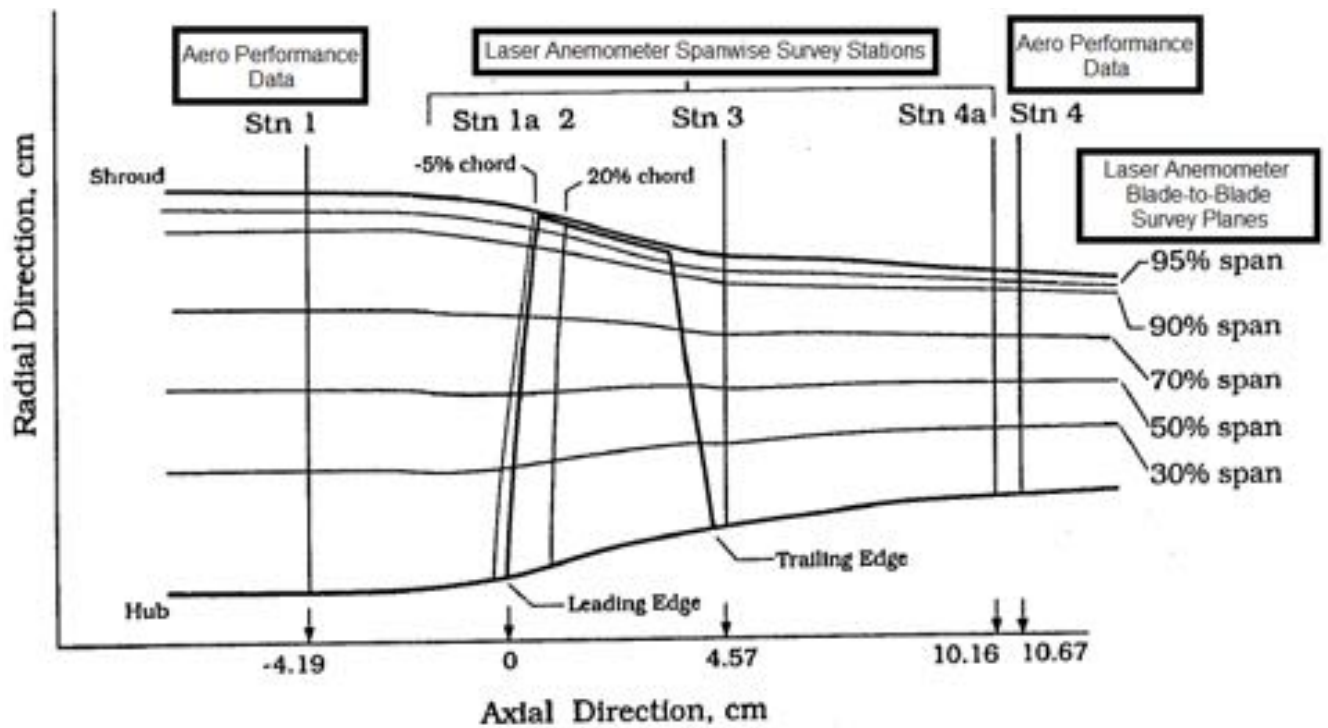


Figure 9 Measurement stations [20]

The overall performance data that were measured over this mass flow rate range are shown on Figure 9. The experimental \dot{m}_{choke} as determined by NASA was 20.93 kg/s. All reported values are equivalent values referenced to sea-level standard atmosphere values of P_{ref} and T_{ref} .

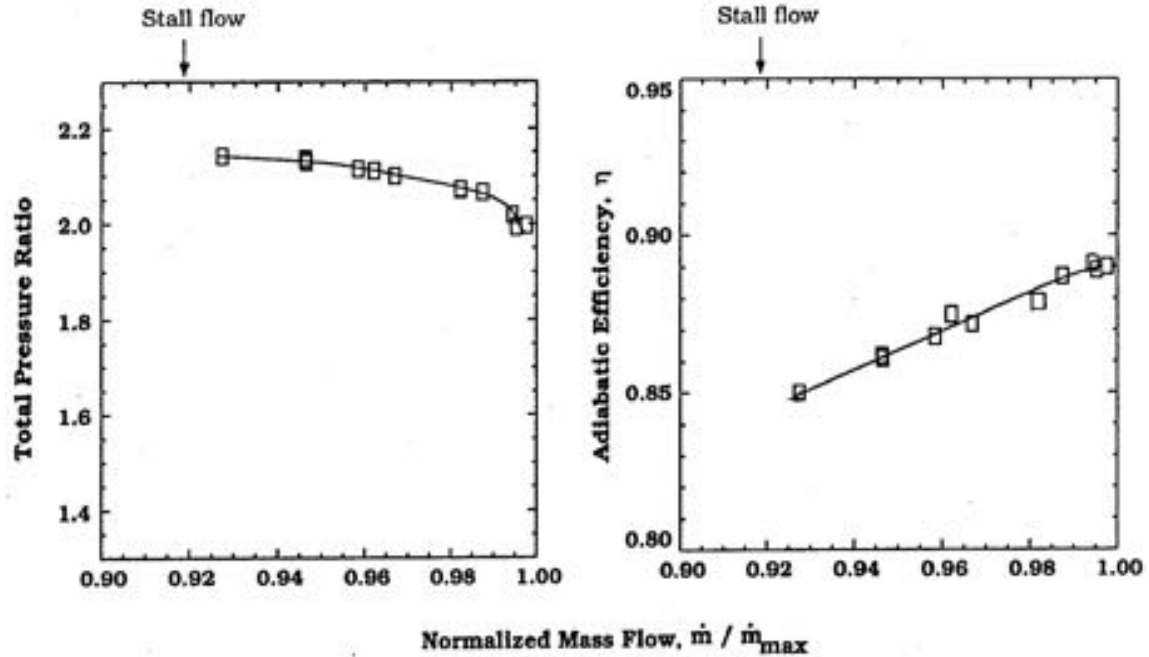


Figure 10 Overall performance at station 4 [20]

The performance data obtained for the NASA Rotor 37 test case included averaged overall total pressure ratio and adiabatic efficiency for a range of equivalent mass flow rates with the rotor operating at equivalent rotational speed (see Figure 10). Mass flow rates were acquired based on the test facility orifice plate measurements. Also, flow passage data were obtained from the radial surveys based on pneumatic pressure probes and thermocouples. [20]

The surveys were at Station 1 and Station 4 (Figure 6). Wall static pressure valves were also recorded by the pressure taps on hub and tip walls at Stations 1 and 4 and turbulence intensity was measured at Station 1. Velocity data sets were recorded at four hub-to-tip measuring planes, as well as on five blade-to-blade surfaces of revolution with the laser anemometer system (Suder et al [58], Suder and Celestina [59] and Hathaway et al [60]). Locations of these planes and surfaces are detailed in Figure 6. Laser data were recorded only at flow rates of $\dot{m}/\dot{m}_{choke} = 0.98$ and $\dot{m}/\dot{m}_{choke} = 0.925$.

Boundary conditions suitable for CFD codes derived from the experimental results are presented in Table 1 (In pg.31). Pressure and temperature ratios P/P_{ref} and T/T_{ref} values from the table can be used as the inlet boundary conditions for a CFD simulation, including the calculation of \dot{m}/\dot{m}_{choke} . The inlet station 1 is $z = -4.19$ cm, while the exit station 4 is $z = 10.67$ cm. The rotor leading edge is at $z = 0$ and hub rotates between $z = 0.246$ cm and $z = 4.521$ cm. In addition, the turbulence intensity at station 1 is 3%, while the hub and tip boundary layers thickness is .82 cm i.e. 10% of the inlet passage height. [20]

Experimental data show a huge dip in total pressure distribution along the span, close to the hub at downstream of the rotor. Most numerical solutions from the blind test exercise did not predict this total pressure deficit accurately and researchers suggest this dip is because the boundary layer separates due to the cavity between rotating blade hub and the stationary blade hub [61, 20]. Ultimately, the Rotor 37 test case was disqualified from the test exercise after a hub leakage flow was identified by Shabbir et al [62]. Later, Chima [63] presented that the hub leakage effect was not a problem, that it does not require any modelling, and the ROTOR 37 test case is an accurate one, suitable for testing competency of the CFD codes.

Table 1 Aerodynamic survey measurement locations and flow conditions at Station 1 [20]

Point	Percentage of span	Radius (cm)	P/P _{ref}	T/T _{ref}
1	97	25.420	0.944	1.001
2	94	25.177	0.976	1.000
3	90	24.841	0.996	1.000
4	85	24.445	1.002	1.000
5	80	24.018	1.004	1.000
6	75	23.622	1.005	1.000
7	70	23.226	1.004	1.001
8	65	22.799	1.003	1.001
9	58	22.250	1.004	1.000
10	51	21.671	1.005	1.000
11	44	21.092	1.005	0.999
12	37	20.544	1.005	0.999
13	30	19.964	1.005	0.999
14	25	19.568	1.005	0.999
15	20	19.141	1.005	0.999
16	15	18.745	1.005	0.999
17	10	18.349	1.004	0.999
18	5	17.922	0.986	1.000

4. METHODOLOGY AND RESULTS

The computational time and resources used to calculate an accurate solution is a key concern in the field of CFD. Accurate prediction of flow properties with the least computational resources is a real challenge and more over flow fields with adverse pressure gradients, and complex structures are even more challenging. To date a large number of research papers have focused on the turbulence models used to solve turbomachinery flows and the computational resources used vary with the turbulence models.

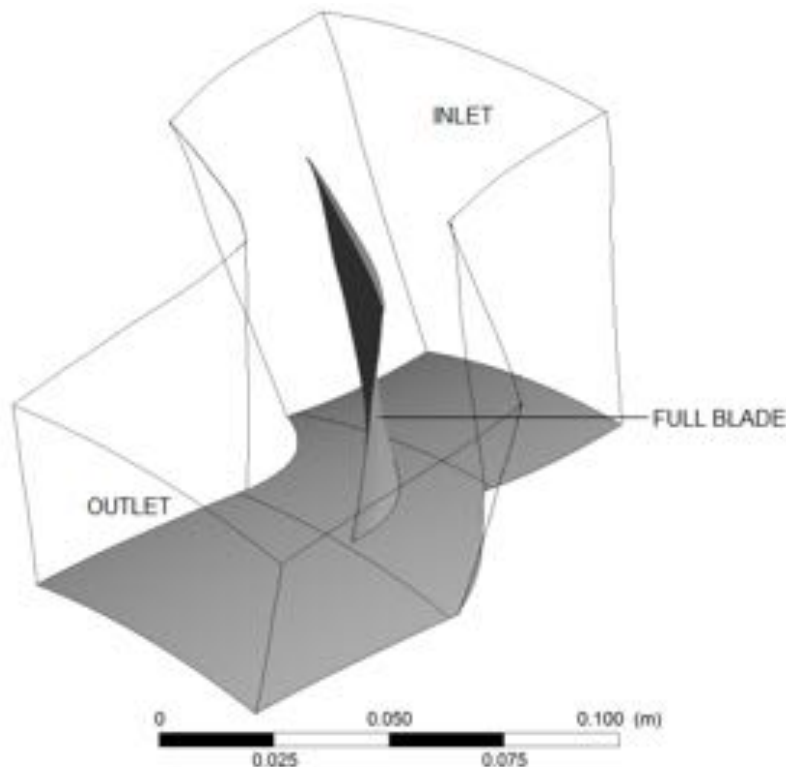
Therefore the effect of turbulence model on the computational resources was not included in this research. The main focus of this research is on how the different methods of modelling the computational domain affect the computational time and resources needed. The computational domain modelling includes flow passage modelling, the interface method used in joining two flow passage blocks, and inlet conditions.

4.1 Numerical modelling

A surface model of Rotor 37 test case was created using CATIA V5. The coordinates of the blade and the test section was imported and modelled with reference to the NASA technical paper [56]. The surface model of the test case was made into multiple blocks for the ease of grid generation. Many models were made during the initial part of the research and after repeated computations, three models were selected for the further analysis. These models are modelled with different numerical modelling techniques for the computational research in this thesis. The models are listed in Table 2.

Table 2 Models description (Model-I, Model-II, Model-II)

MODEL-I	Modelled, similar to the test case. The fluid flow around the rotating blade is modelled. This model was used in previous researches.
MODEL-II	The blade was split and the passage between the blades were modelled. The tip-face was attached to one side of the blade. Attaching the tip-face to one side of the blade was never before. Modified for the current research to reduce the complexity of the domain geometry and so in grid generation.
MODEL-III	Similar to the MODEL-II, the passage between the blades were modelled and the tip-face was completely eliminated. This model was introduced to check for the possibility of eliminating the tip-face to further reduce complexities in the computation.



ANSYS
R14.5
Academic

Figure 11 MODEL-I (Complete Blade)

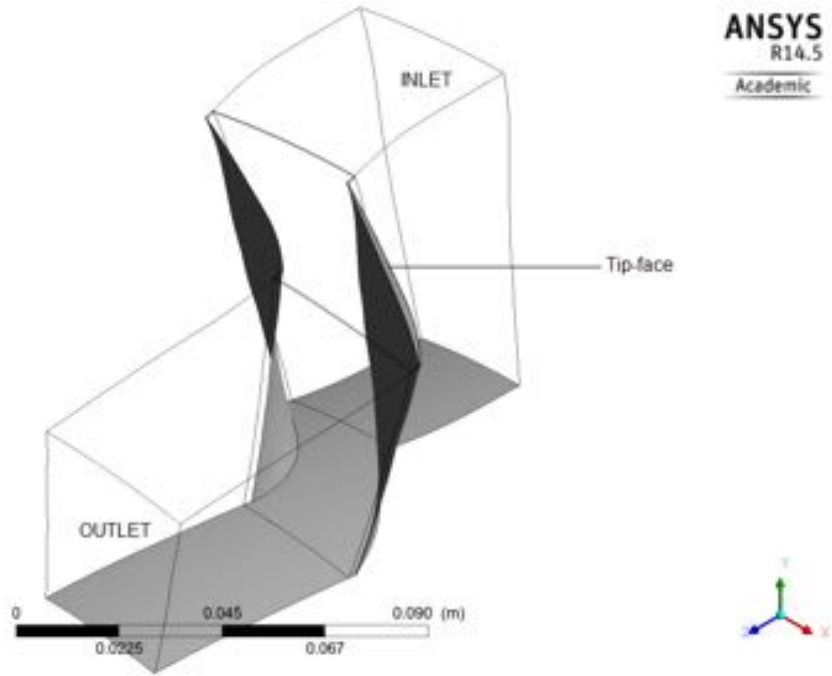


Figure 12 MODEL-II

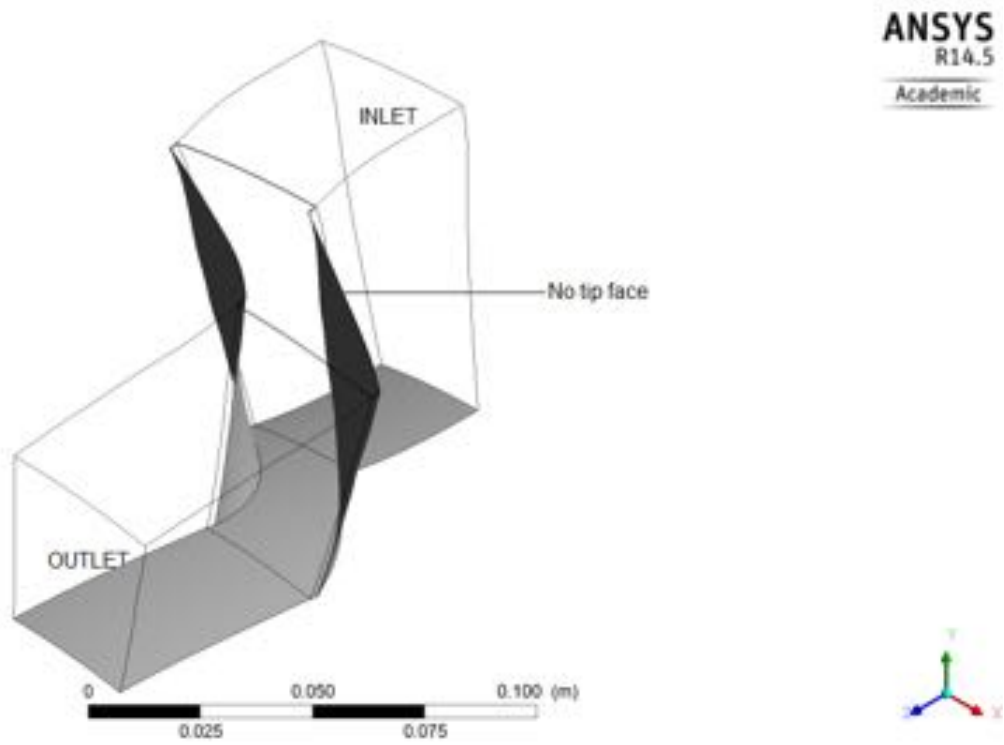


Figure 13 MODEL-III

The commercial CFD code ANSYS-CFX 14.5 was used to develop the numerical model of the aerodynamic behaviour of Rotor 37. The three-dimensional RANS equations were solved by means of the finite volume method. In order for the numerical model to be well defined, an investigation was carried out to determine the effects of grid density on the accuracy of the solution. This was done simulating the flow field of Rotor 37 using models I and II with varying grid density, and comparing predictions with the published experimental data.

Comparisons were made in terms of both total pressure ratio to normalised mass flow rates and adiabatic efficiency to normalised mass flow rates. For all the models a multi-block structured grid was used to discretize the computational domain i.e. Model-I with 4 blocks, Model-II with 5 blocks and Model -III with 4 blocks. The number of blocks each domain was made into depends on the geometry of the domain, and the blocks are detailed in Table 3.

Table 3 Models with multidomain structured grid

Models	Number of blocks	Blocks location/Name (Grid type)
Model-I	4	Inlet block (H Grid), Blade passage block (O-H Grid), Tip block (O-H Grid) and Outlet block (H Grid).
Model-II	5	Inlet block (H Grid), Blade passage block (H-C Grid), Tip passage block (H grid), Tip-face block (H grid) and Outlet block (H Grid).
Model-III	4	Inlet block (H Grid), Blade passage block (H-C Grid), tip passage block (H Grid) and Outlet block (H Grid).

The computational domains were modelled as a single blade passage with rotational periodic boundary conditions on the lateral faces. Inlet and outlet boundaries correspond to Station 1 and Station 4 of Figure 6 respectively. The total pressure, total temperature, and absolute flow angle of the incoming flow were fixed at the inlet boundary, while the average static pressure of the delivered flow was imposed at the outlet (the boundary pressure profile is a result of the computation).

In order to reproduce the boundary conditions of the above-mentioned Rotor 37 test facility, the inlet total pressure profile and total temperature profile was imposed using Table 1. The walls were treated as smooth and adiabatic. An angular velocity corresponding to the equivalent rotational speed of Rotor 37 was applied. For each simulation, the convergence criterion was established when normalized root mean square (RMS) residuals were less than 10^{-6} .

The Shear Stress Transport $k - \omega$ turbulence model, designed to give highly accurate predictions for the turbomachinery applications, was adopted to solve all the models. All model grids were refined at the walls to have a near-wall grid resolution of $y^+ \leq 1$, needed to guarantee a strict low-Reynolds number model implementation. The grids were adequately refined to eliminate the wall-functions. Steady-state simulations were conducted for the all the models in the current thesis. All simulations were made possible by the facilities of the Shared Hierarchical Academic Research Computing Network (SHARCNET: www.sharcnet.ca) and Compute/Calcul Canada.

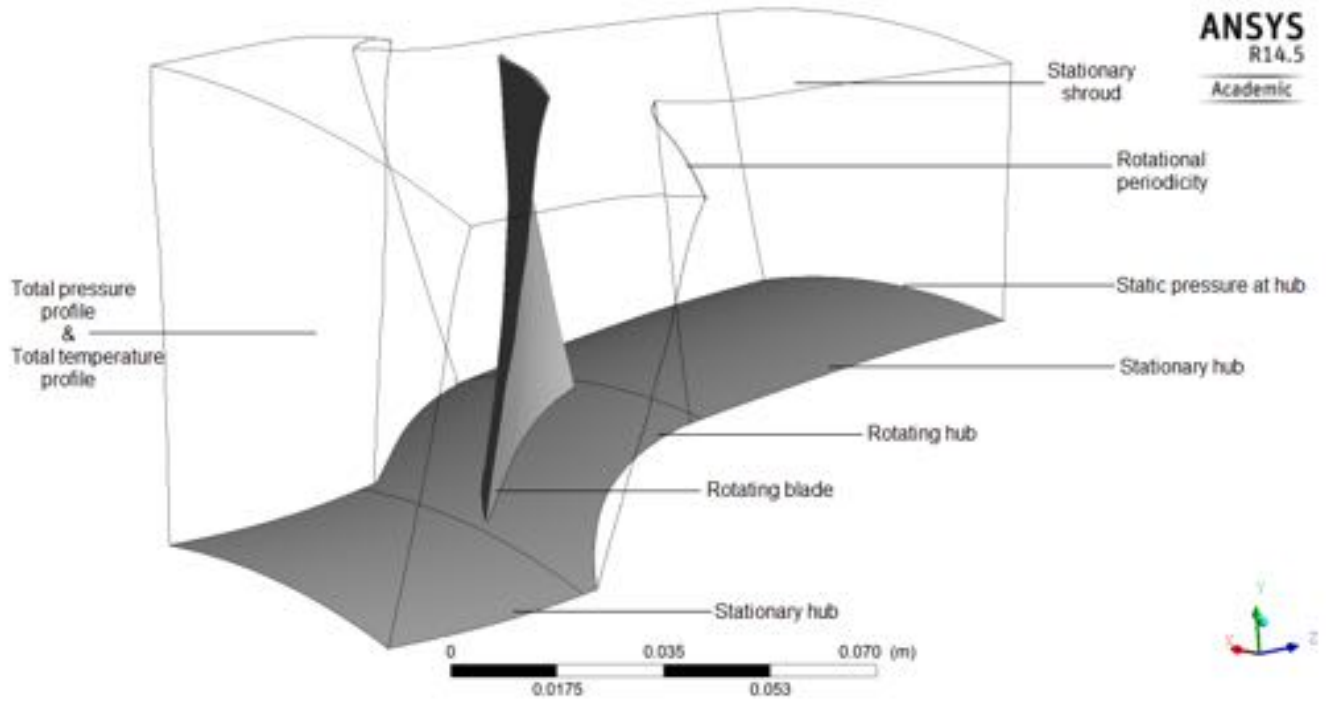


Figure 14 Model-I with Boundary conditions

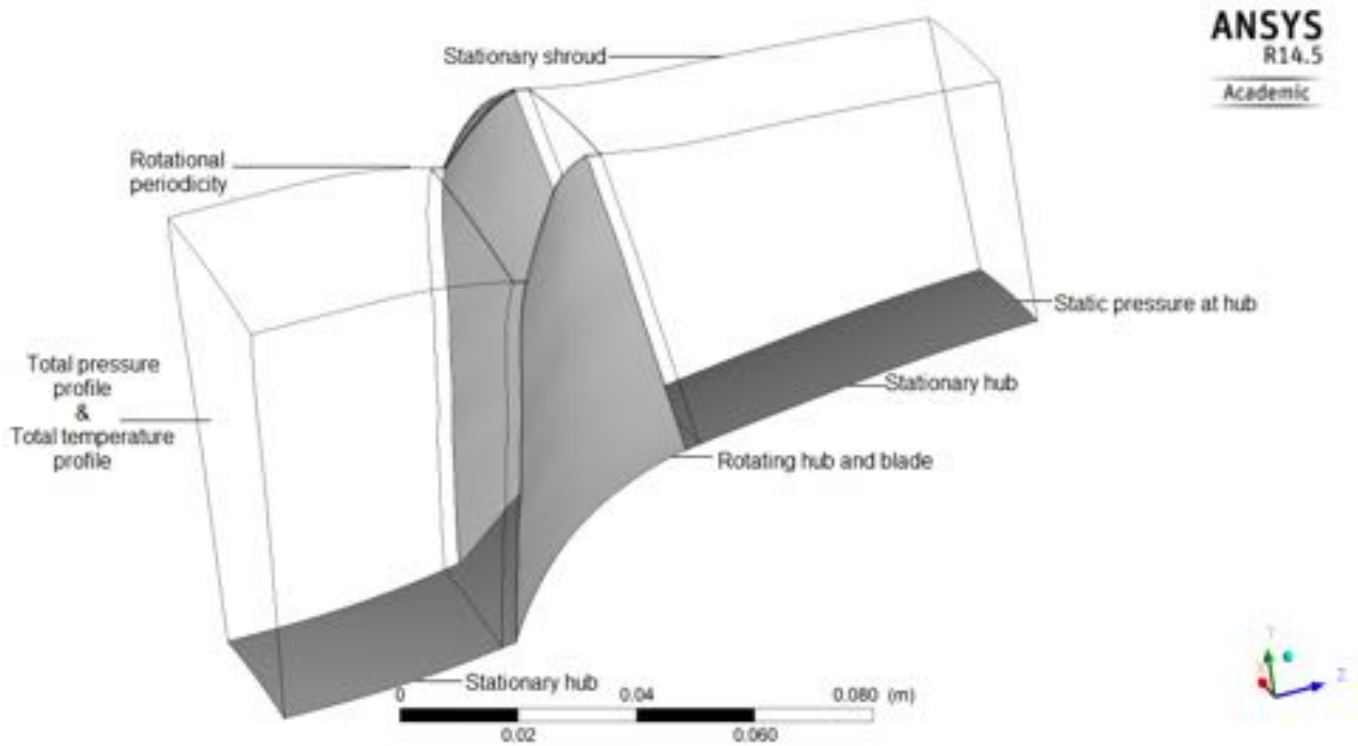


Figure 15 Model-II with Boundary conditions

4.1.2 Effect of Grid density

Three sub-models under each model (Model-I and Model-II) were created with varying grid density and the grids were adequately refined to eliminate the wall-functions. A suitable grid density for Model-III can be estimated from the grid study made on the other two models. The sub-models are:

Table 4 Sub-models for grid density study

Models	Grid type with $y^+ \leq 1$	Number of nodes in millions	Turbulence Model
Model-I A	Structured - 4 blocks	1.4	SST
Model-I B	Structured - 4 blocks	1.8	SST
Model-I C	Structured - 4 blocks	2.2	SST
Model-II A	Structured - 5 blocks	1.2	SST
Model-II B	Structured - 5 blocks	1.4	SST
Model-II C	Structured - 5 blocks	1.8	SST

For each model the total pressure ratio (P_{04}/P_{01}) and the adiabatic efficiency η was calculated. These values were calculated by varying the static pressure at the outlet (Note: the static pressure is specified on the hub at the outlet) was varied, while the inlet pressure profile and the average

static pressure were held constant. Repeated numerical simulations were performed to determine the conditions for choked flow. The total pressure ratio and adiabatic efficiency was plotted with respect to the corresponding normalized mass flow rates.

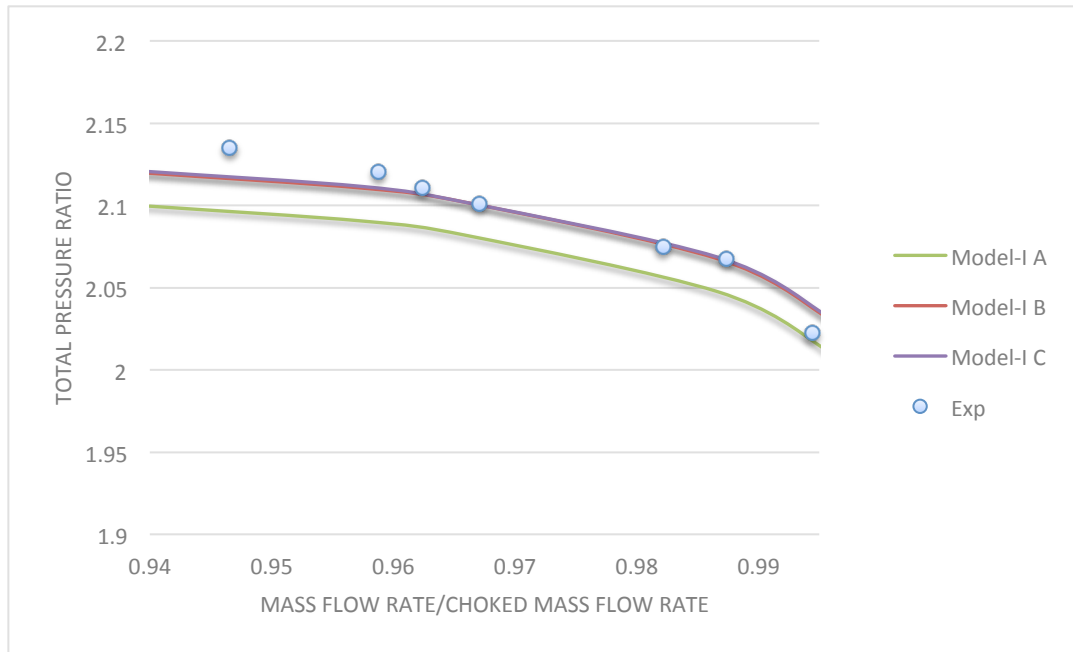


Figure 16 Total pressure ratio Vs. Normalized mass flow rate for Model-I A, B, and C

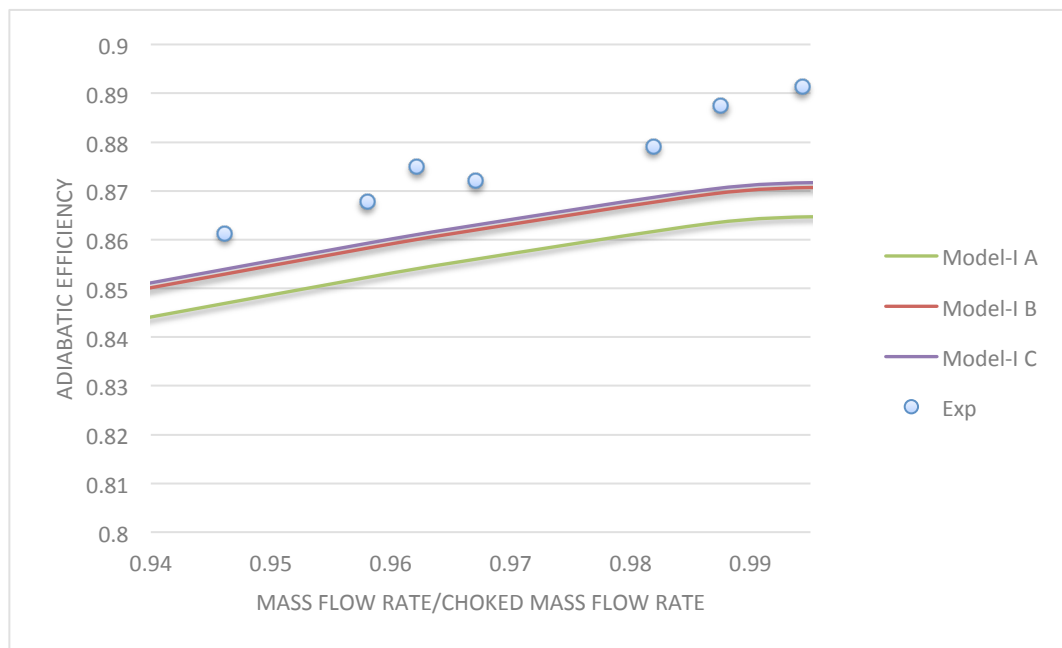


Figure 17 Adiabatic efficiency Vs. Normalized mass flow rate for MODEL-I A, B, and C

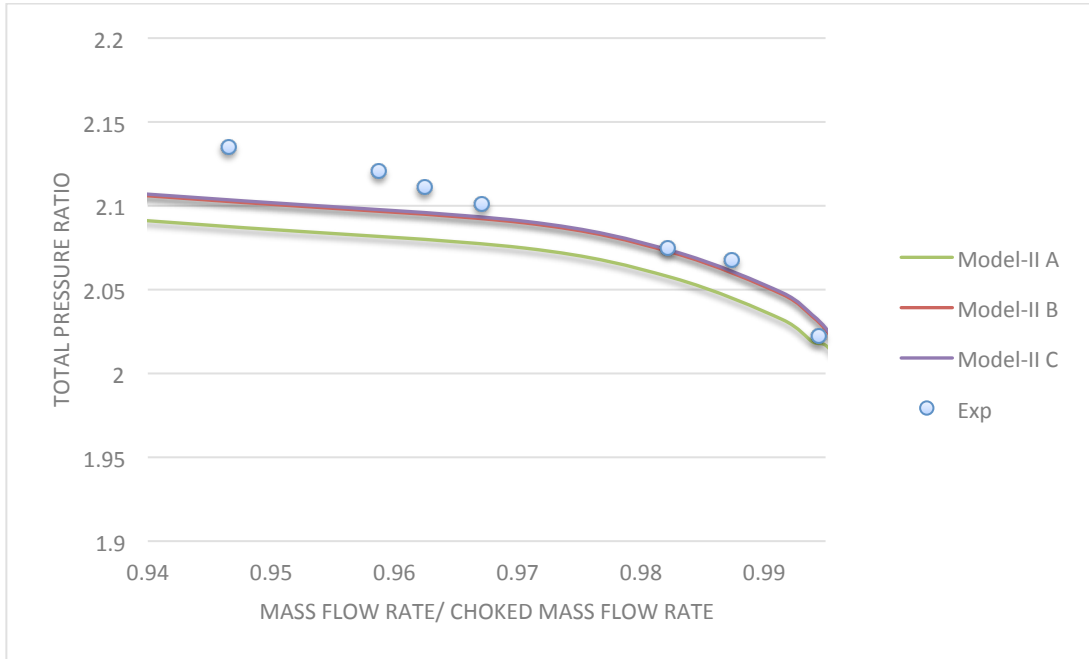


Figure 18 Total pressure ratio Vs. Normalized mass flow rate for MODEL-II A, B and C

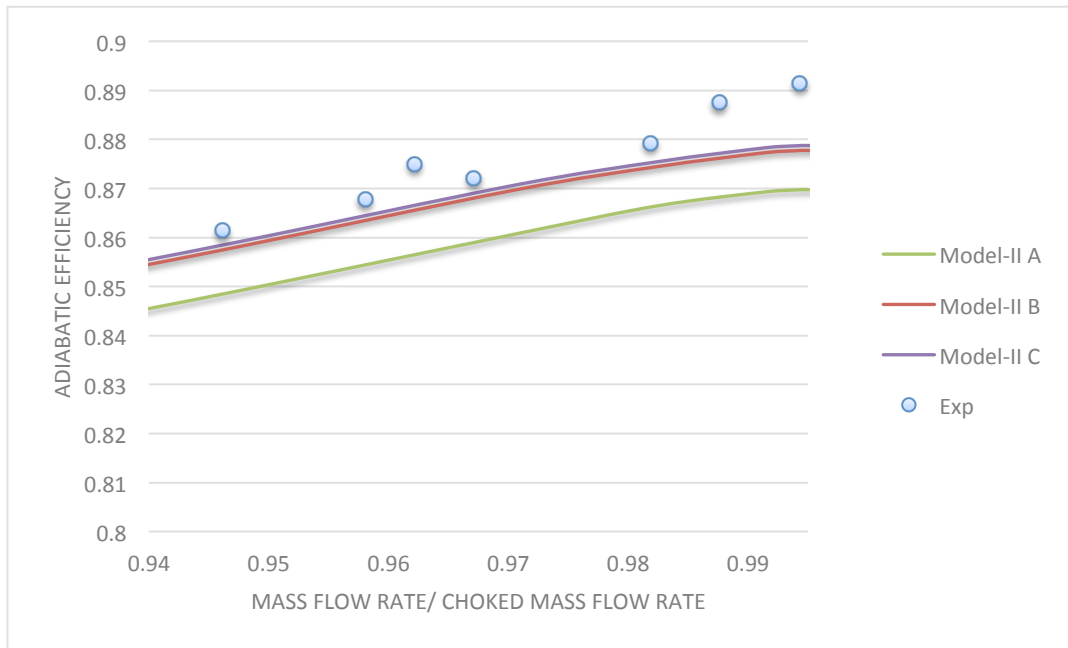


Figure 19 Adiabatic efficiency Vs. Normalized mass flow rate for MODEL-II A, B and C

All the six models closely predicted the shape of the experimental curve in Figures 13-16 (experimental data is labelled as Exp in the figures). Comparing the results, Model-I did not show further improvements in the prediction of total pressure and adiabatic efficiency when the number of nodes was increased from 1.8 million to 2.2 million. Similarly, Model-II did not show any improvement in the prediction of total pressure and adiabatic efficiency when the number of nodes was increased from 1.4 million to 1.8 million. Considering the fact that lesser computational time is required for solving a lesser number of nodes, Model-I B and Model-II B were considered for the further study in the following sections. The nodes distribution for the main three models are tabulated in Table 5.

Table 5 Grid construction

Models	Structured multi blocks number of nodes (X x Y x Z), The grids near the walls are refined to yield $y^+ \leq 1$, All grids are very smooth at the interfaces of the blocks.					Number of nodes in millions
	Inlet block	Outlet block	Blade passage block	Tip passage block	Tip-face block	
Model- I B	50x80x60	60x70x90	60x140x90	60x140x50	-	1.8
Model- II B	50x80x60	60x70x90	60x100x75	60x100x30	40x30x100	1.4
Model- III	50x80x60	60x70x90	60x100x75	60x100x30	-	1.2

In all the blocks, three dimensional grids were constructed from sweeping two-dimensional grids along the Y axis. To create the two dimensional grids, the nodes were defined on the edges (along X and Z axes) of the face to be swept. The nodes are biased depending on the smoothness required at the block interfaces. The swept faces were biased and the faces on the blades were inflated. The biasing and inflations were iterated until $y^+ \leq 1$ was satisfied. The multi block structured grids for the Model-I B and Model-II B are shown in Figures [20-23]. The grid space for the Model-III was adopted from Model-II B by eliminating the tip-face block.

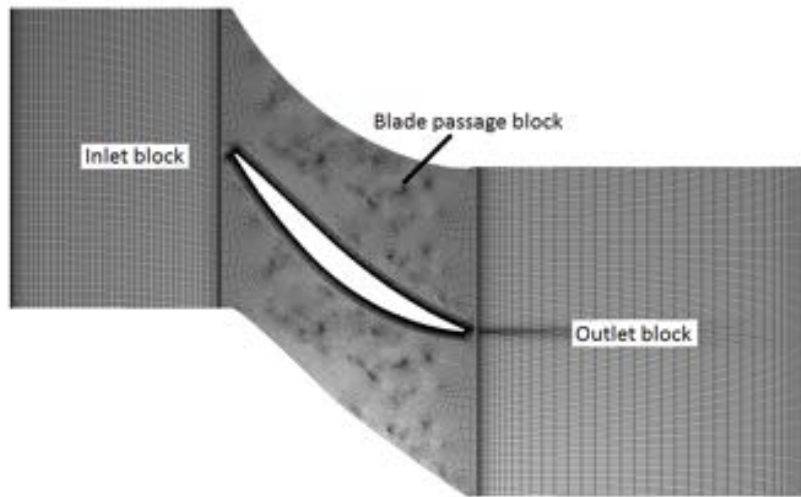


Figure 20 Model-I B grid distribution on the hub

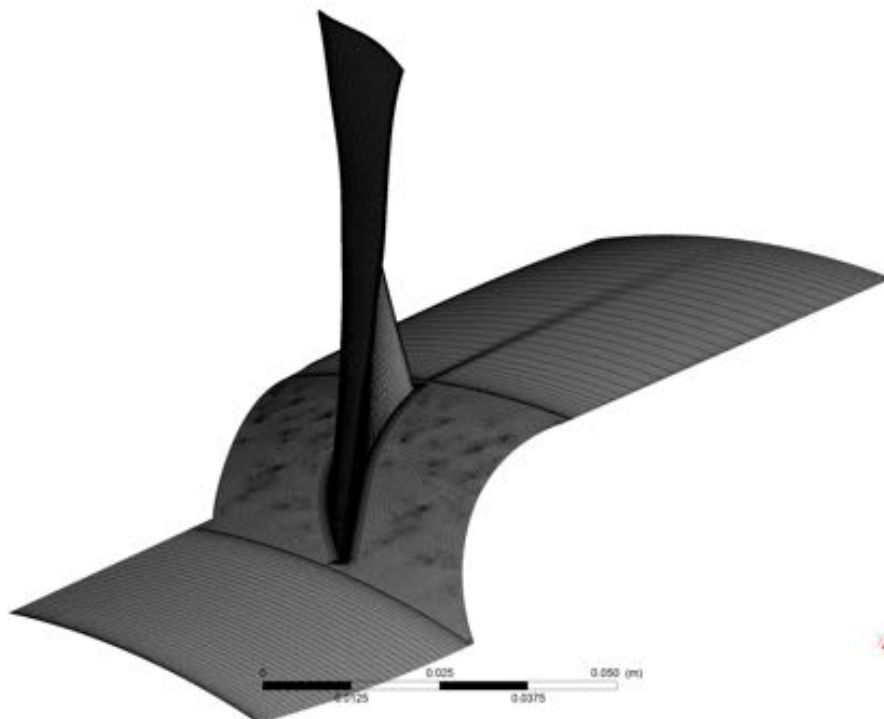


Figure 21 Model-I B grid distribution along the blade and hub

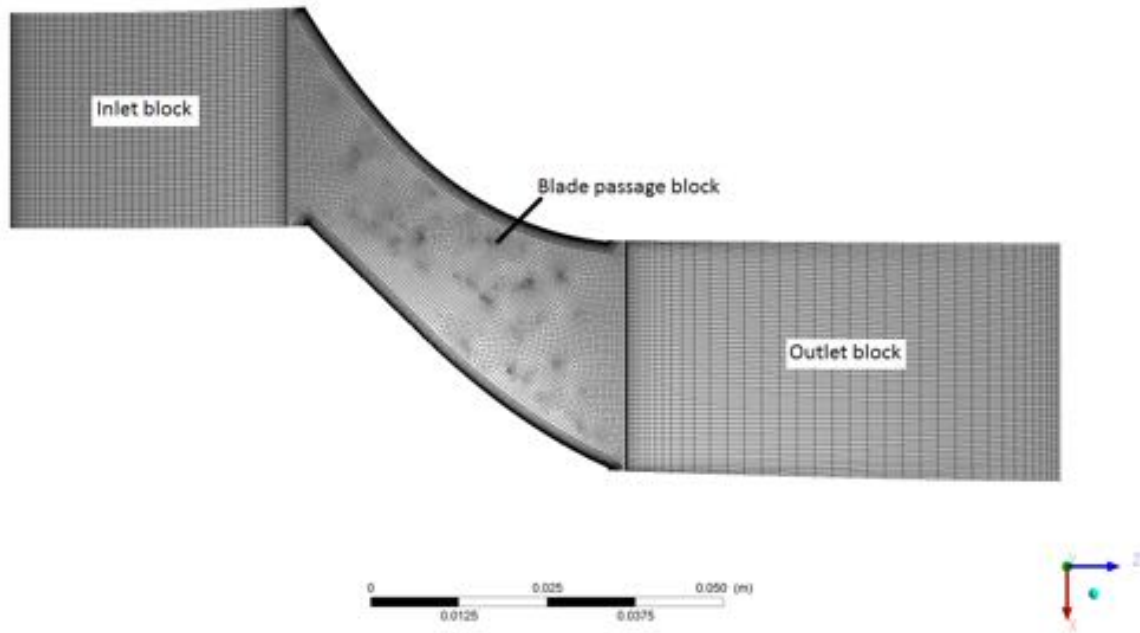


Figure 22 Model-II B grid distribution on the hub

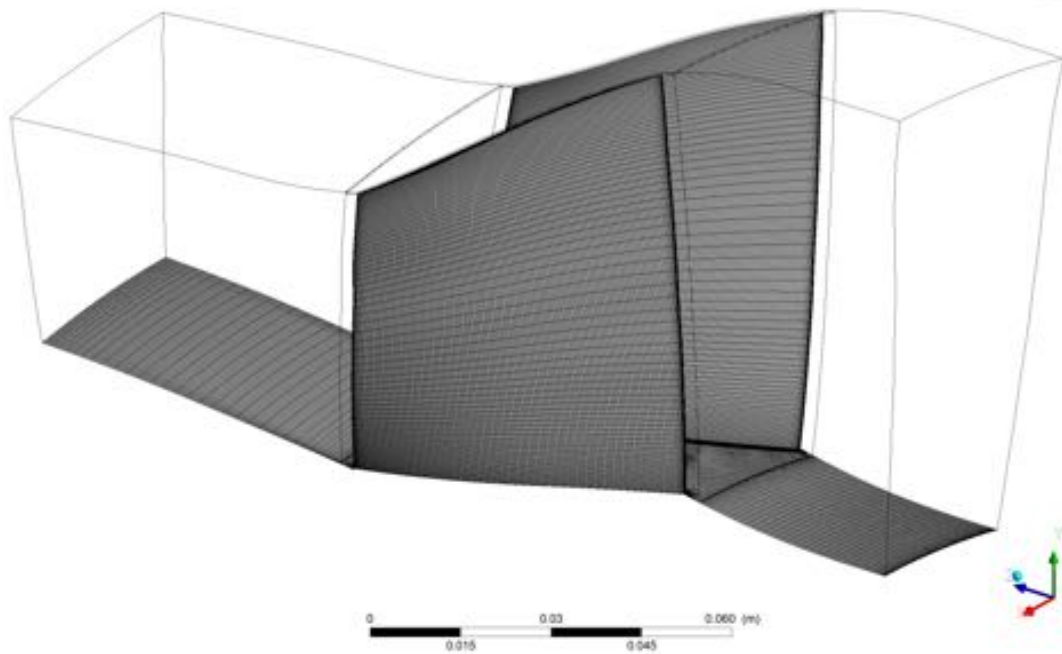


Figure 23 Model-II B grid distribution along the blade and hub

4.2 Performance assessment

For the initial assessment, all the three models i.e. Model-I B, Model-II B and Model-III were used. More focus was placed on analysing the predictions at 98% of the choked flow operating conditions (near peak efficiency). The problems of analysing the simulated results are due to the shortage of plotted quantities in the experimental and the simulated results. For example, the insufficient knowledge about the axial velocity component, both from experimentally measured and also from predicted results, had led to difficulties in velocity triangle analysis. To deduce a firm conclusion for the comparisons between the experimental and CFD results, AGARD [20] recommended two main sets of data for the CFD validation of propulsion systems. They are:

Blade-to-blade contour plots of relative Mach number at different percentages of the blade height (especially at 70% of the blade height); pitch wise plots of relative Mach number after the trailing edge, at stations 3 and 4, and at 20% chord inside the rotor at station 2.

Radial plots of circumferentially averaged quantities at station 4. Most prior researchers have plotted the absolute stagnation pressure P_{o4}/P_{o1} , the absolute stagnation temperature T_{o4}/T_{o1} , and the adiabatic efficiency.

4.2.1 Computational Performance of Model-I B and Model- II B

All the three models were solved for conditions varying from choked flow to a near stall. The total pressure ratio, total temperature ratio, adiabatic efficiency, total pressure ratio (P_{o4}/P_{o1}) and total temperature (T_{o4}/T_{o1}) variation along span at near peak conditions (98% of choked mass flow rate) were plotted for assess modelling accuracy.

All the three models used the total pressure profile and total temperature profile at the inlet shown in Table 1. The static pressure at hub was used as the outlet condition. The entire model is set to be rotating at the equivalent rotational speed of 17188.7 rpm (1800 rad/s). The stationary walls were defined as counter-rotating i.e. only the blades, hub and tip face will be considered as rotating wall and the rest are considered as stationary with respect to the rotating walls. The frozen rotor method was adopted to model the interface between the blocks and an RMS value of 10^{-6} was set as convergence criteria. High Resolution Advection Scheme and SST turbulence model was used. The numerical models were solved using 8 parallel processors in parallel. The choked mass rate is identified from repeated computational runs by varying the static pressure at the outlet.

The detailed numerical domain of Model-II B is shown in Figures 17-20 as this model is new and has never been demonstrated before. The general connection with no frozen rotor method is used at interface between the tip-face block and tip-passage block (Figure 17, 18), while the frozen rotor method at all stator-rotor interfaces. Closer view of the rotational periodicity on the lateral face is shown in Figure 19 and tip-face in Figure 20. Model-I B took 3.81 hours while Model-II B took 2.72 hours for the solution to converge. The computed choked mass flow rate was approximately 20.56 kg/sec with 10% boundary layer thickness at the inlet, which is the same as the mass flow rate predicted by Ameri [64].

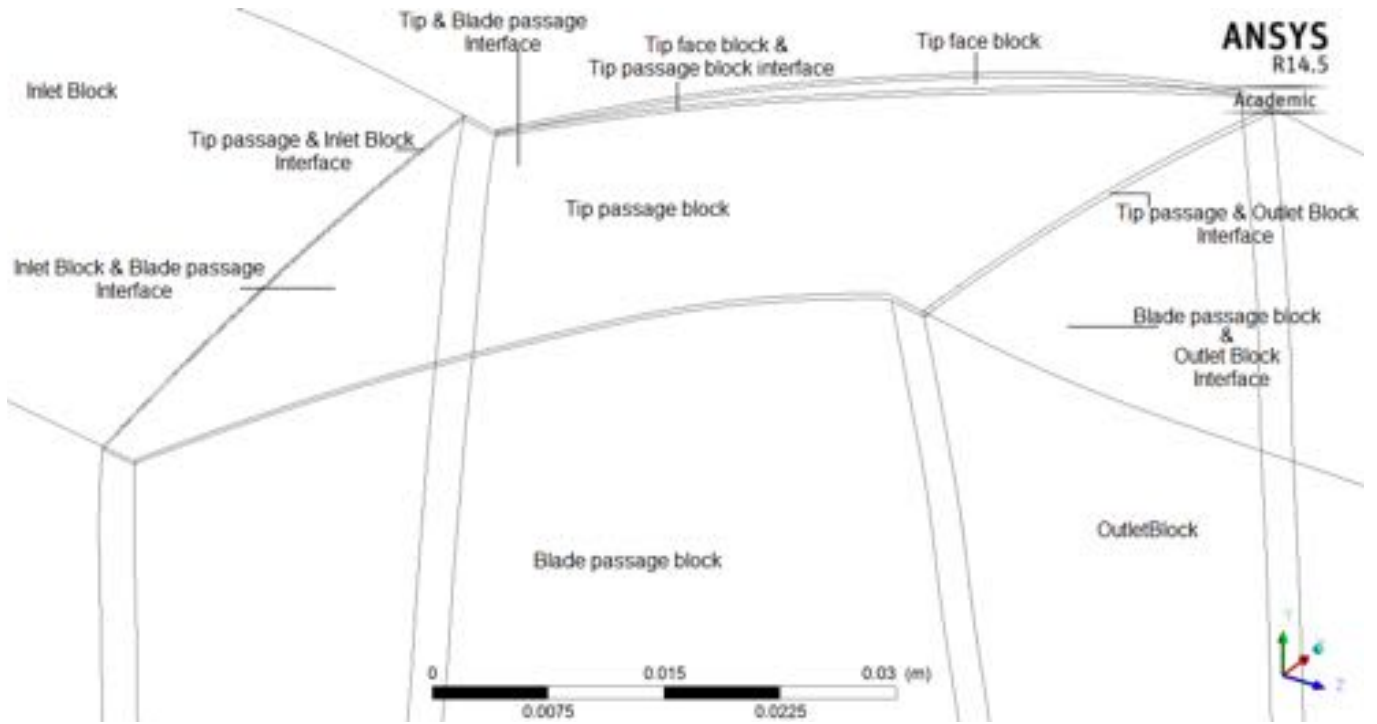


Figure 24 Detailed view of computational domain Model-II B

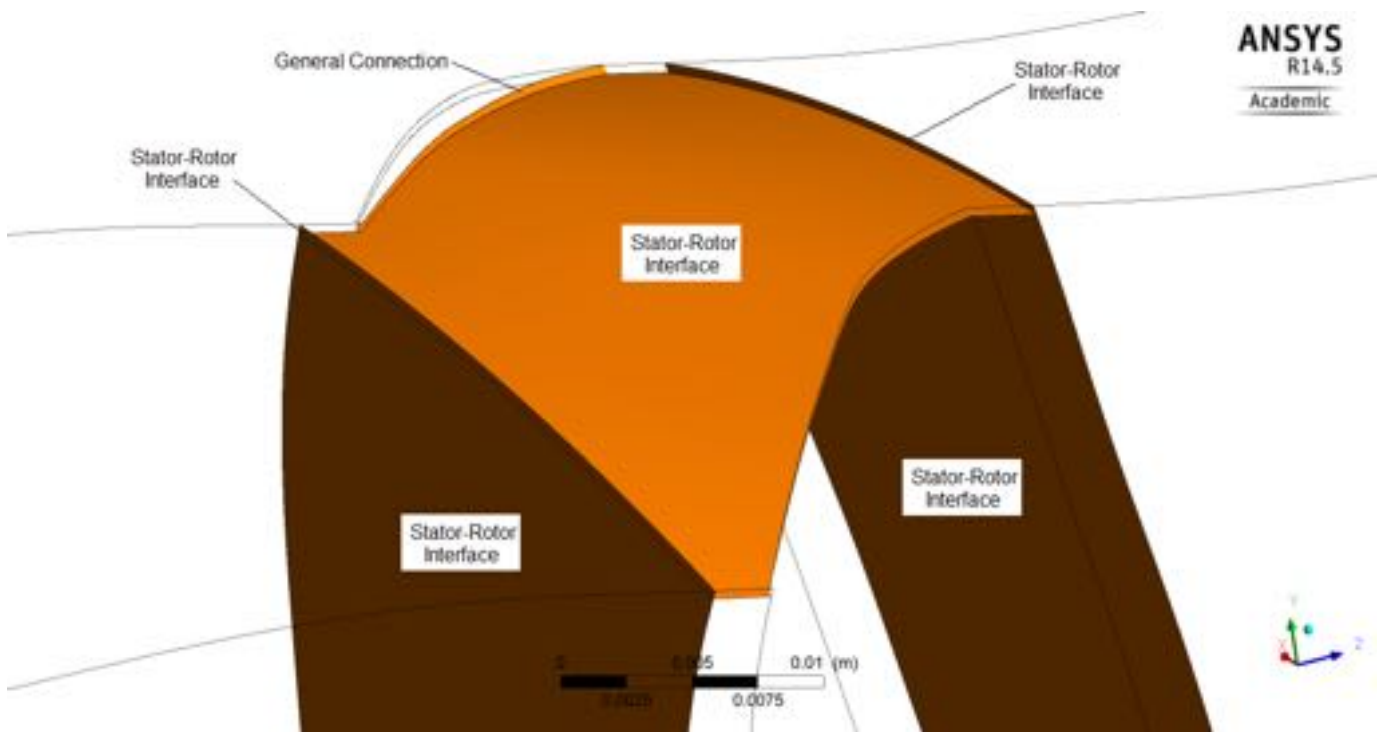


Figure 25 Block interfaces in Model-II B

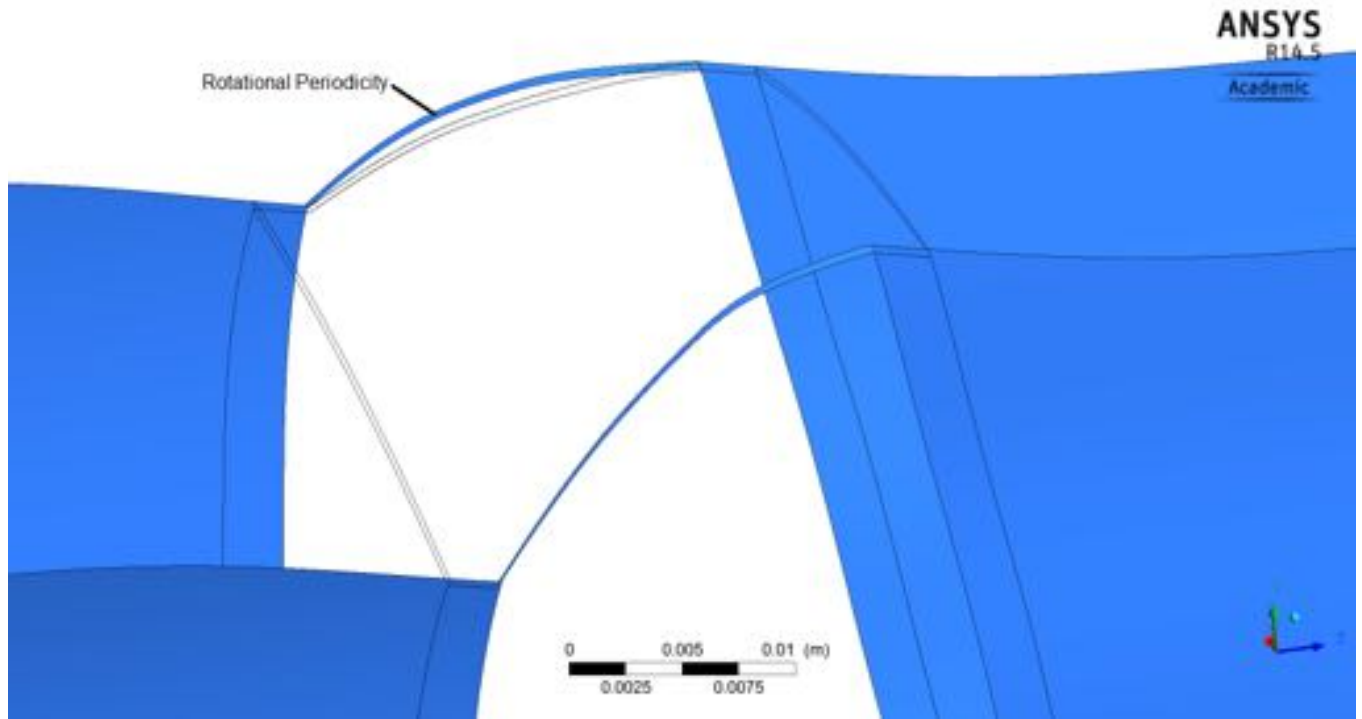


Figure 26 Periodic condition - rotational periodicity (Model-II B)

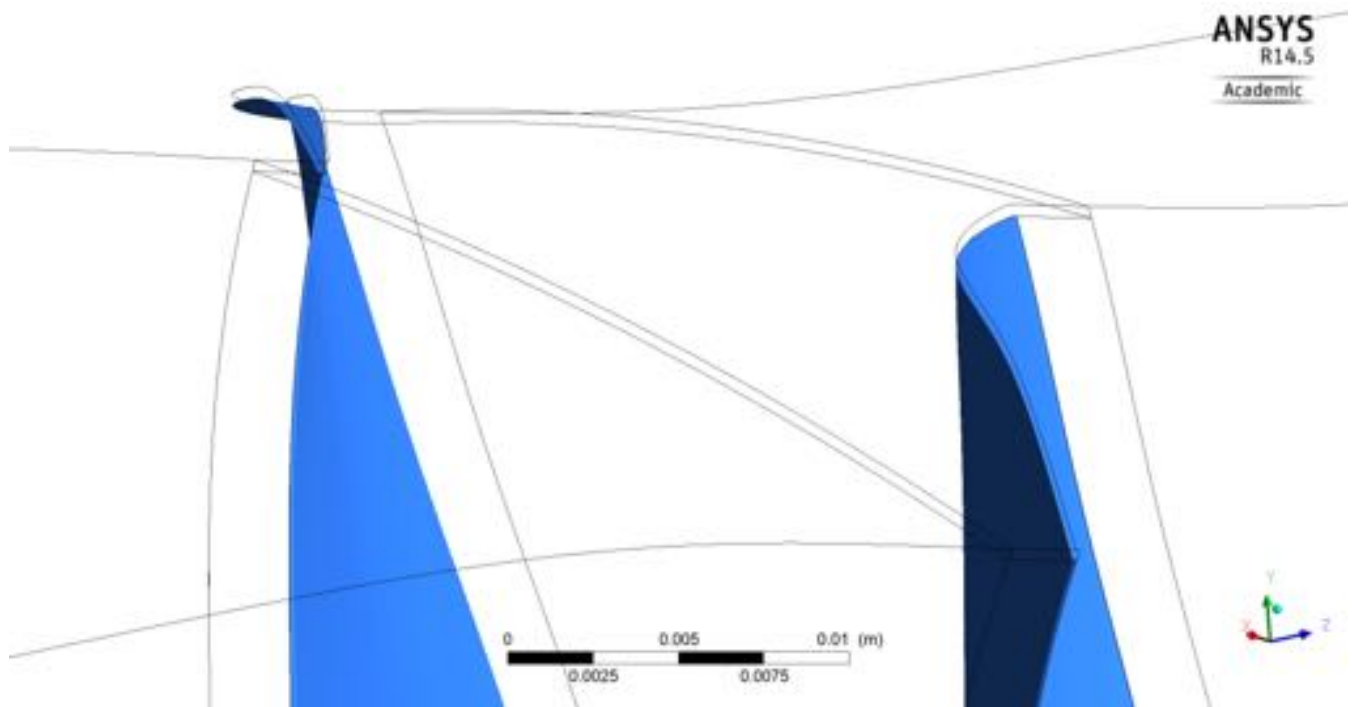


Figure 27 Closer view of the tip-face (Model-II B)

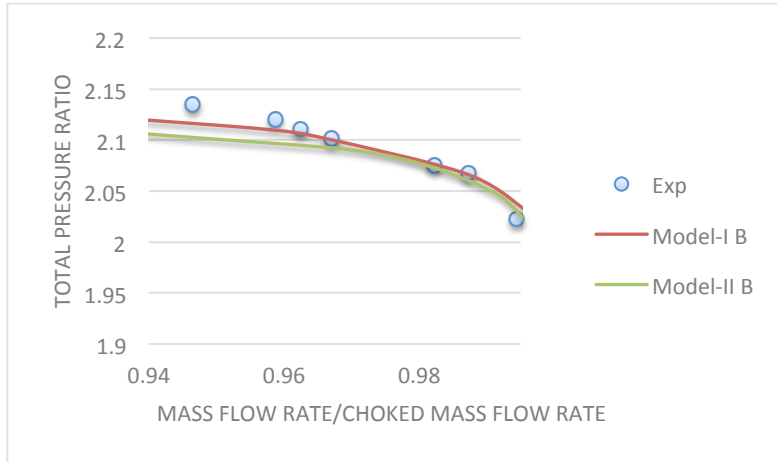


Figure 28 Total pressure ratio Vs. Normalized mass flow rate (Model-I B and Model-II B)

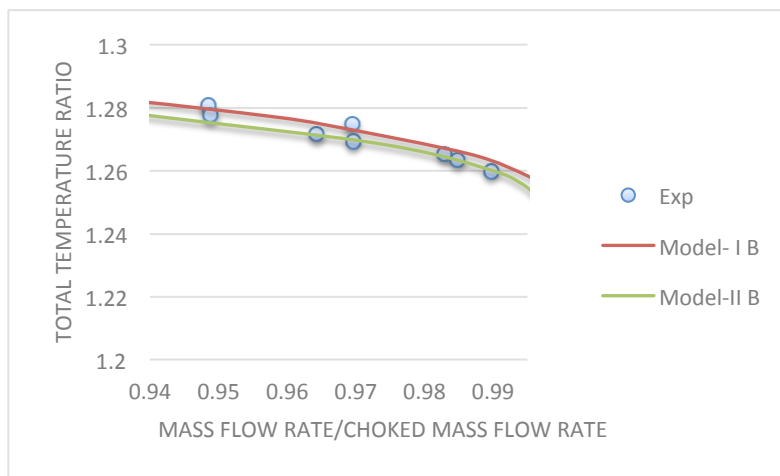


Figure 29 Total temperature ratio Vs. Normalized mass flow rate (Model-I B and Model-II B)

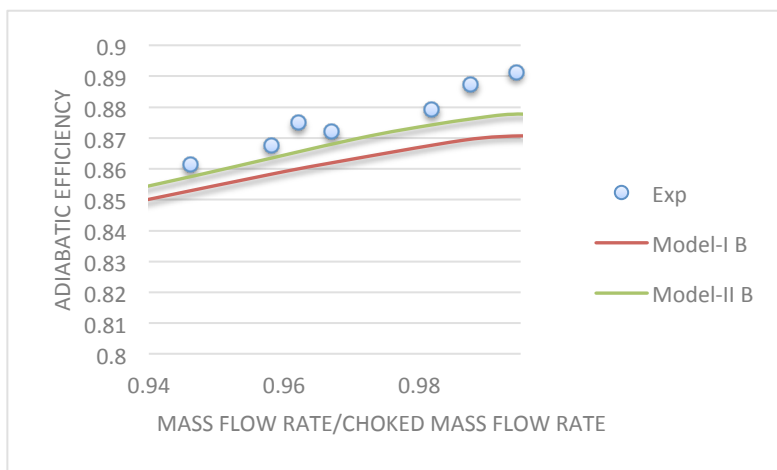


Figure 30 Adiabatic efficiency Vs. Normalized mass flow rate (Model-I B and Model-II B)

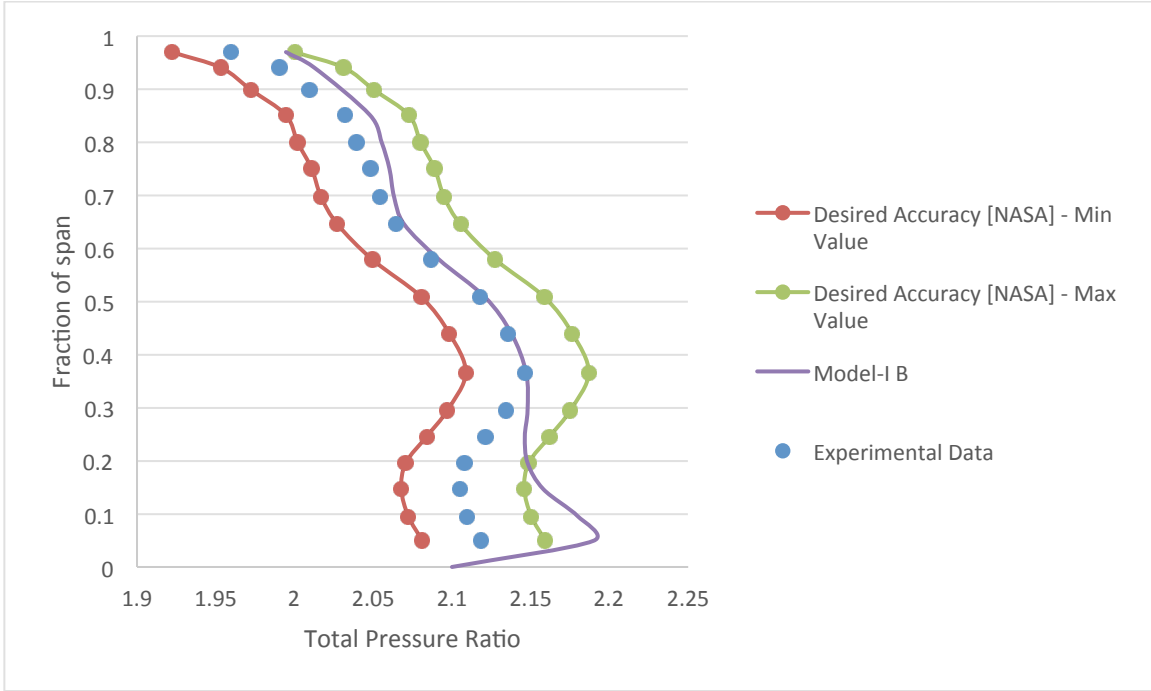


Figure 31 Total pressure ratio along span at station 4 (Model-I B)

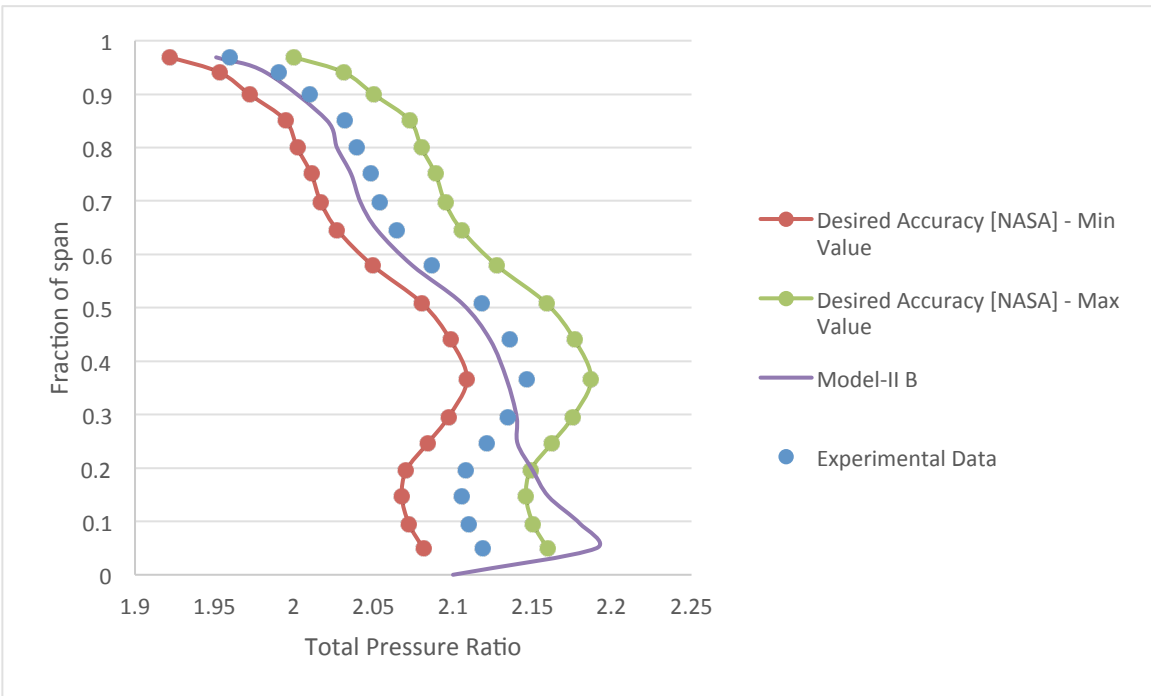


Figure 32 Total pressure ratio along span at station 4 (Model-II B)

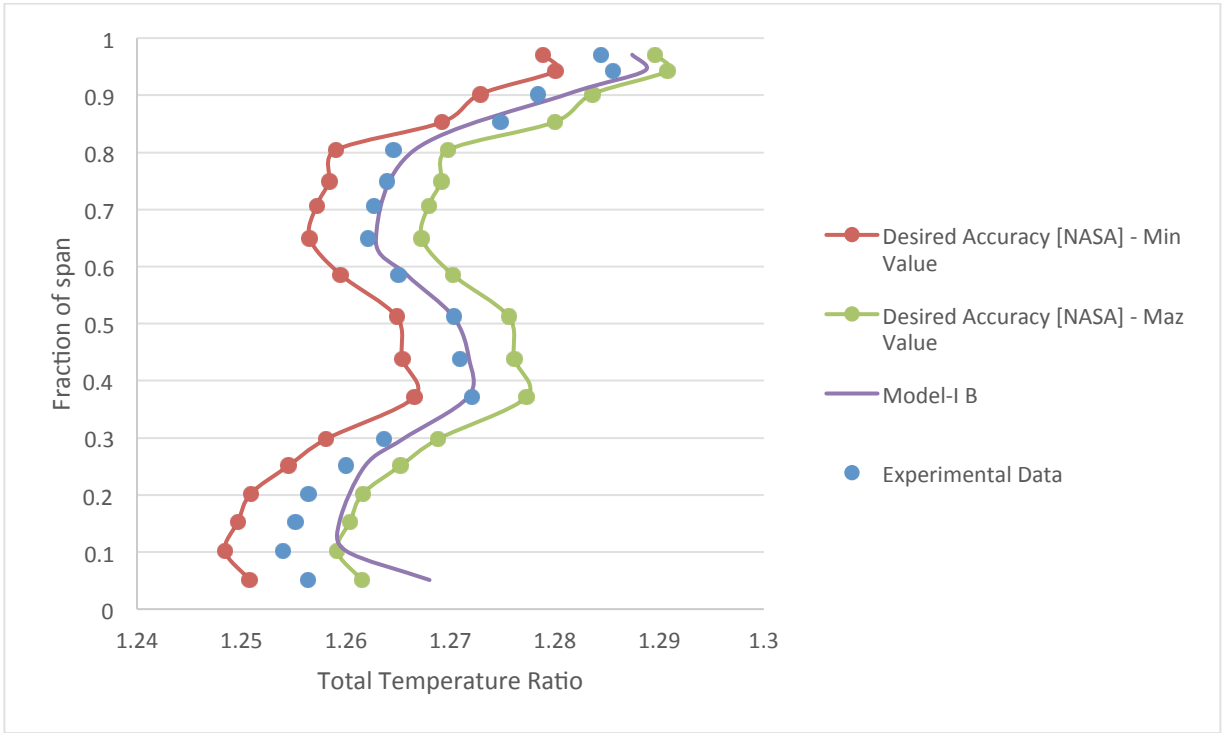


Figure 33 Total temperature ratio along span at station 4 (Model-I B)

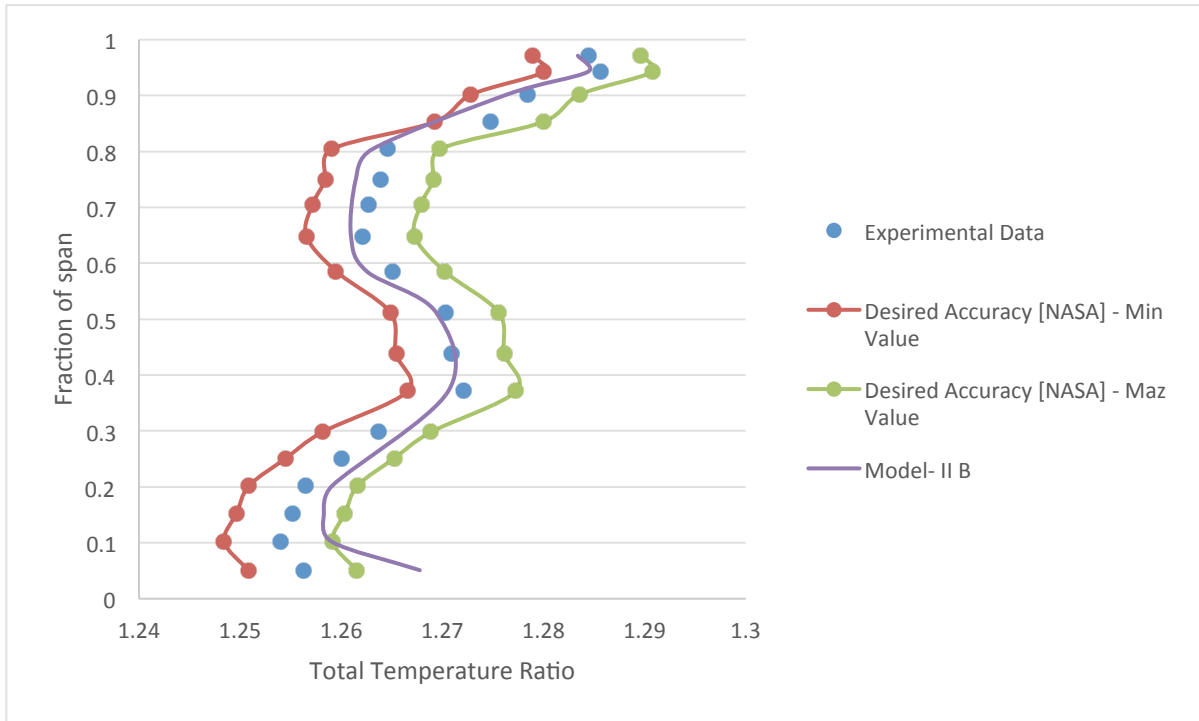


Figure 34 Temperature ratio along span at station 4 (Model-II B)

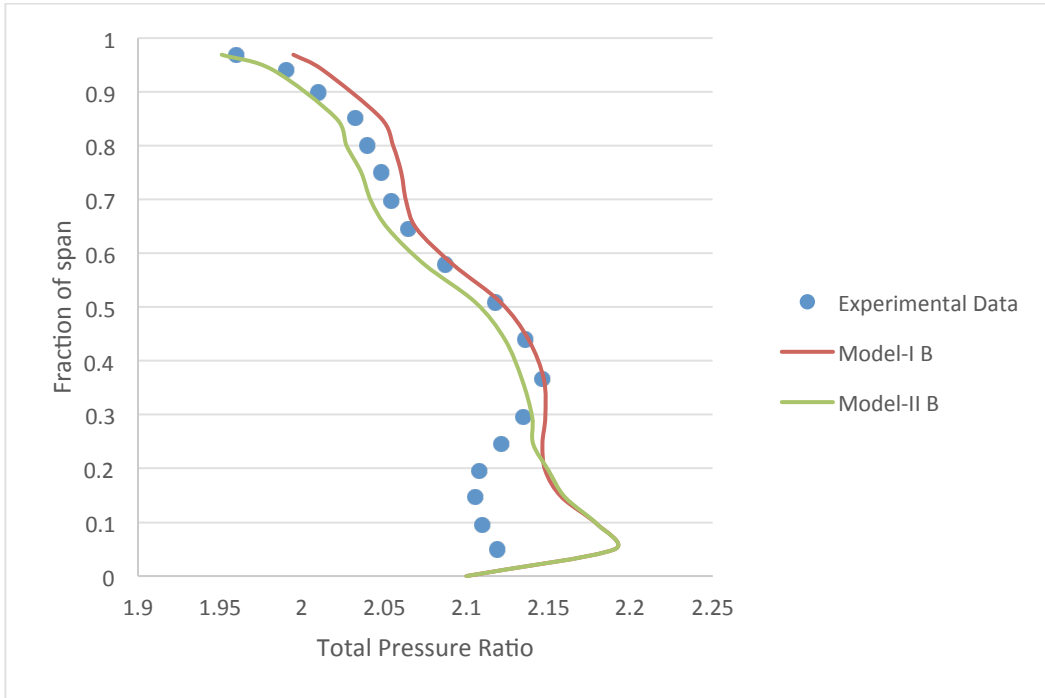


Figure 35 Total pressure ratio along span comparison between Model-I B and II B

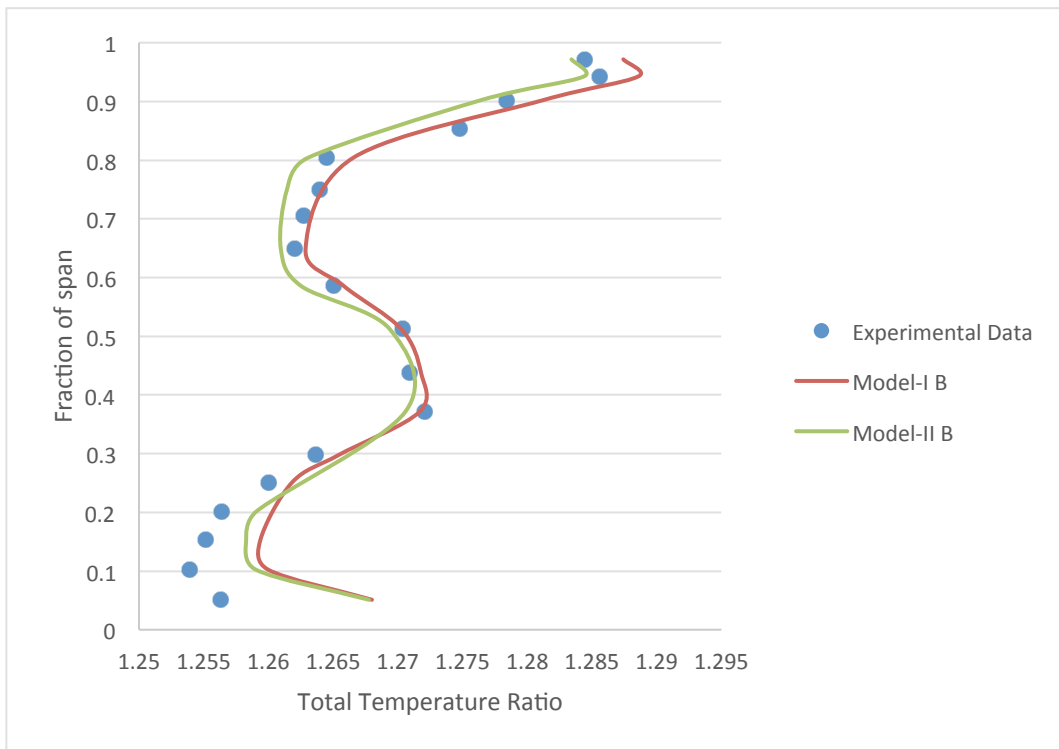


Figure 36 Total temperature ratio along span comparison between Model-I B and II B

Comparing the variation of flow properties with respect to the mass flow rate from Figures 28-30, all the models accurately captured the shape of the experimental data curves of the flow. The values predicted were very close to the experimental results. Model-I B predicted values slightly better than the Model-II B near the stall conditions. The Model-I B performed better in the low flow conditions because of the denser grid. However Model-II B predicted the adiabatic efficiency better than Model-I B.

The predicted total pressure ratio and total temperature ratio along the span for both the models are within the desired accuracy [Figure 31-36] limits suggested by Glenn Research Centre, NASA [64]. Both the models failed to capture the shape of the experimental results close to the hub in the radial performance plots. The predicted total pressure ratio below the 40% span [Figure 28] did not match the experimental curve. This could be due the hub leakage effect as suggested by Shabbir at al [62]. The temperature ratio and pressure ratio predicted by Model-I B close to shroud (casing) is higher than the experimental values. This divergence was also noticed in all the results published in the AGARD report [20] and researchers predicted it was because of a large separation region within the casing boundary layer. Larger boundary layer separations could be due to the adverse pressure gradient and the interaction between passage shock and clearance vortex [61]. However Model-II B predicted the values close to the experimental values, better than the model-I B. It is believed that Model-II B predicted with better accuracy because of the regular and less skewed passage grid in the tip-face block and tip-passage block, as explained by Chima [63] and Ameri [64] that the under prediction of losses are due to the irregularly spaced and skewed grids near the tip region.. Figure 37 illustrates the difference in tip gap modelling between the typical Model and Model-II B. Figure 37.1 and 37.3 shows the well-spaced and less-skewed grid elements, whereas the grids in Figure 37.2 are highly-skewed

because of the complexity in the geometry. In this case the grids are more skewed when the tip face is split into two halves. In Model-II B as the complete tip face is attached to one side of the blade it reduces the complexity in geometry and provides more flexibility for creating the grids.

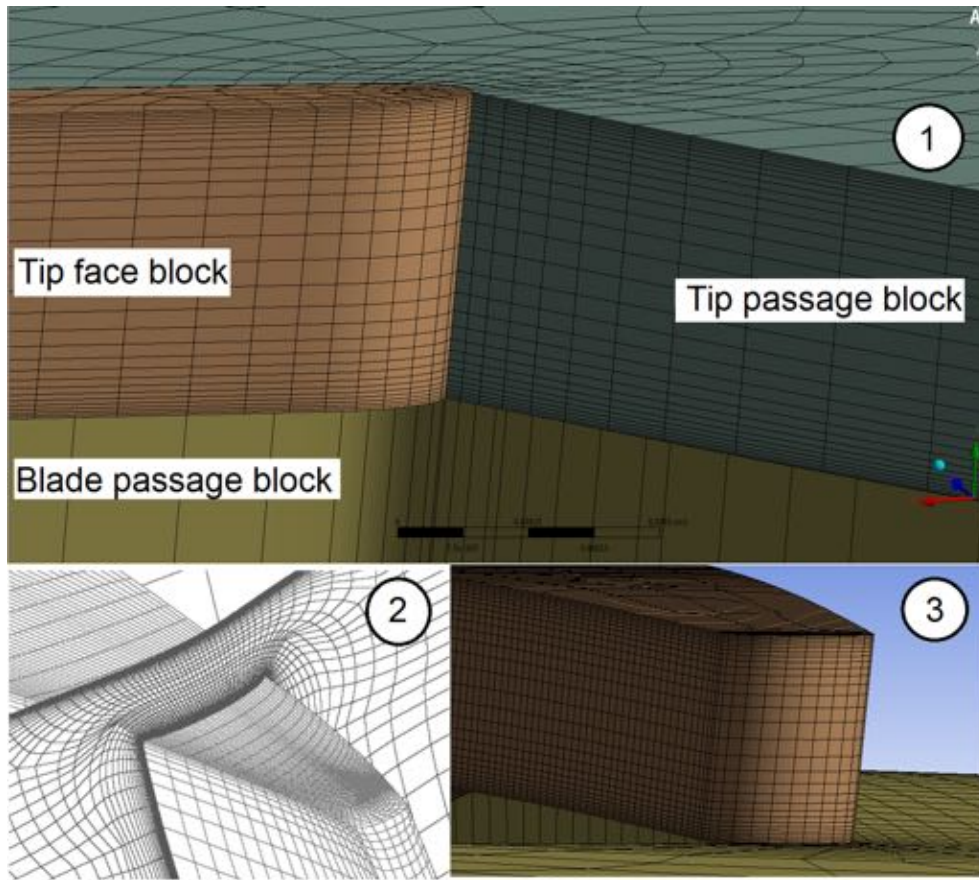


Figure 37 Comparison of computational grid between Model-II B and other models

The other validation method and an aid to understand the flow is the blade to blade Mach number contour plot. The solution at 70% span section for Model-I B and Model-II B, in terms of Mach number for the near peak efficiency or the operating condition is shown in Figure 39-40. Both Models closely resembles the shock pattern seen in the experimental result in Figure 38. The shocks were well captured at the leading edge but the amount of shock smearing depends more on the number of grid points in this region than the numerical method [65].

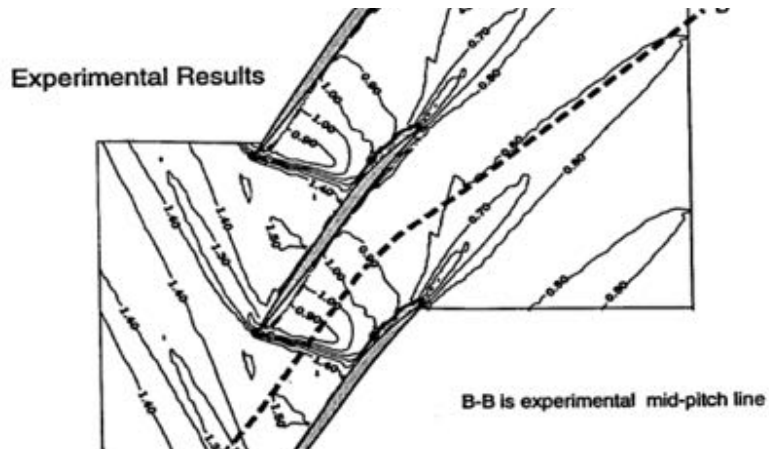


Figure 38 Blade-Blade Mach number contour at 70% span and 98% choked flow for experimental data [61]

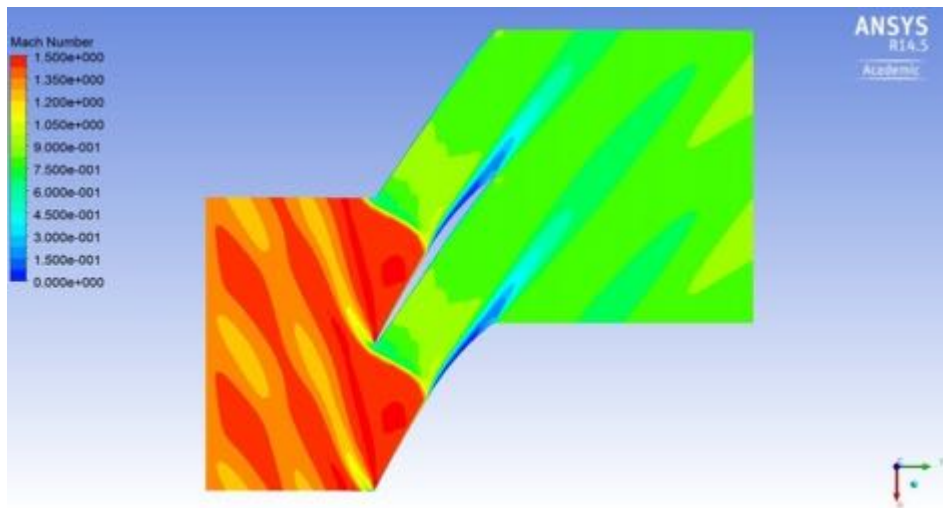


Figure 39 Blade-Blade Mach number contour at 70% span and 98% choked flow (Model-IB)

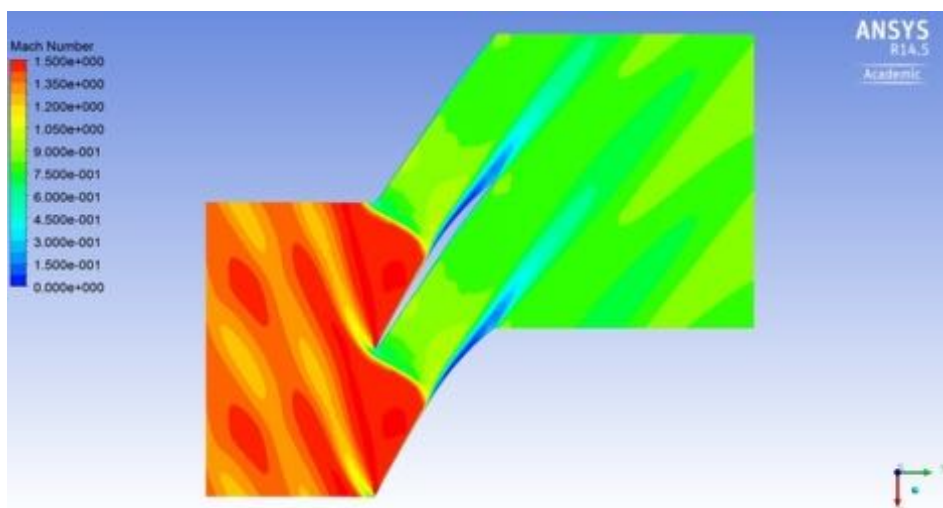


Figure 40 Blade-Blade Mach number contour at 70% span and 98% choked flow (Model-II B)

Many models used by previous researchers over predicted the overall pressure ratio because of the increased shock pressure rise and because flow separation at the trailing edge was too low [66]. These factors directly affect the prediction of the overall pressure ratio. Both the models (I B and II B) predicted the boundary layers well enough to get the overall pressure ratio close to the experimental results.

4.2.2 Performance of Model-III

The Model-III (with no tip face) was solved by varying the static pressure at the outlet and with the boundary conditions similar to the other models. The computed choked mass flow rate was 20.563 kg/s and was achieved at $P_{\text{static}} = 113000$ kPa defined at the outlet. The choked mass flow rate was 0.367 kg/s less than the original case. The computational grid density for Model-III was adopted from Model-II B as the flow domain of the two models were largely the same. Model-III consists of 1.2 million nodes.

The total pressure ratio, temperature ratio and adiabatic efficiencies are solved for the normalised mass flow rate varying from the choked condition to near stall condition. Model-III took 2.38 hours for the solutions to converge and the computational setup is shown in Figure 34. Table 6 shows the predicted results with decrease in the mass flow rate. The usual tendency of the rotors is to produce high pressure ratio at low mass flow conditions but the result predicted by Model-III (with no tip-face) has only a marginal increase in pressure ratio from 95% of choked flow to 90% of choked flow.

Table 6 Computational Results of Model-III

mdot	mdot/ mdot choke	Po4/Po1	Adiabatic Efficiency	To4/To1	
20.563	1.000	1.998	0.8727	1.251	Choked
20.542	0.999	2.008	0.8730	1.253	
20.495	0.997	2.025	0.8729	1.256	
20.398	0.992	2.046	0.8717	1.260	
20.095	0.977	2.067	0.8651	1.266	Near Peak
19.663	0.956	2.071	0.8539	1.271	
18.637	0.906	2.089	0.8320	1.282	

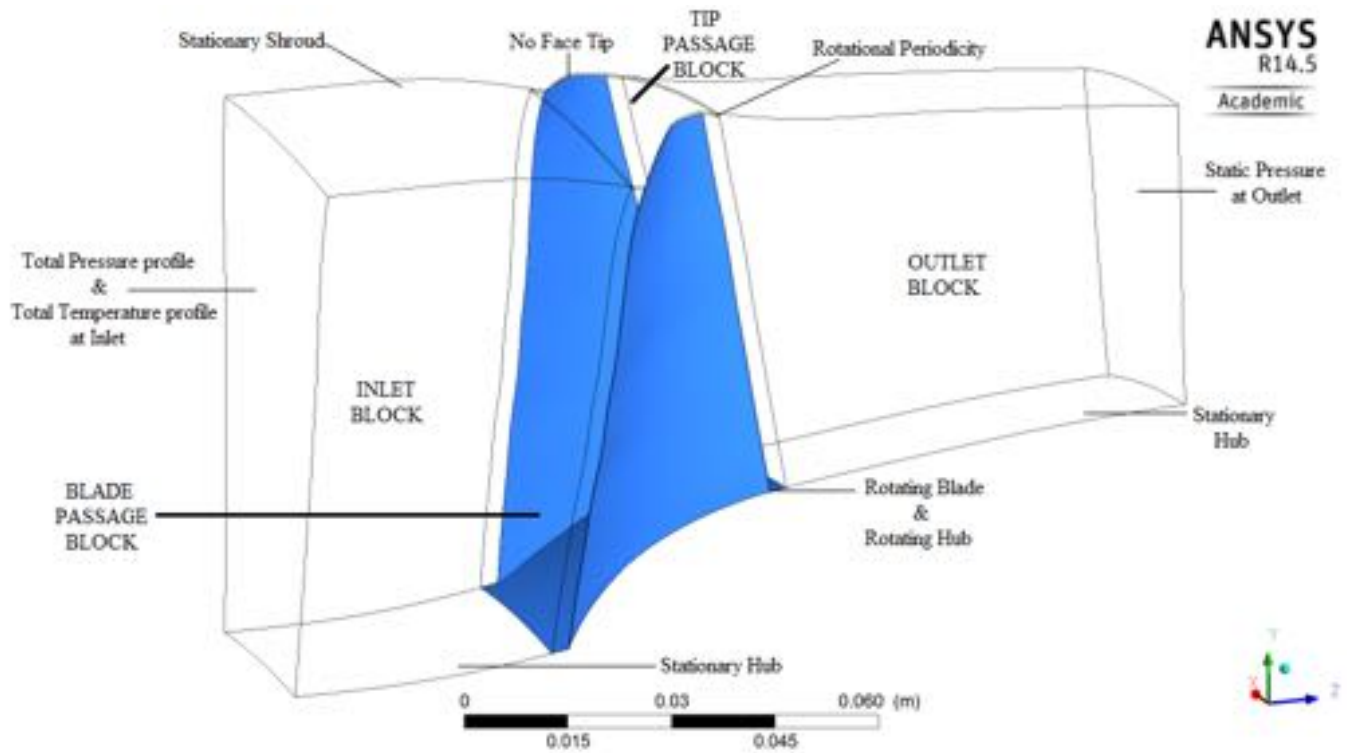


Figure 41 Computational domain of Model-III (No face tip)

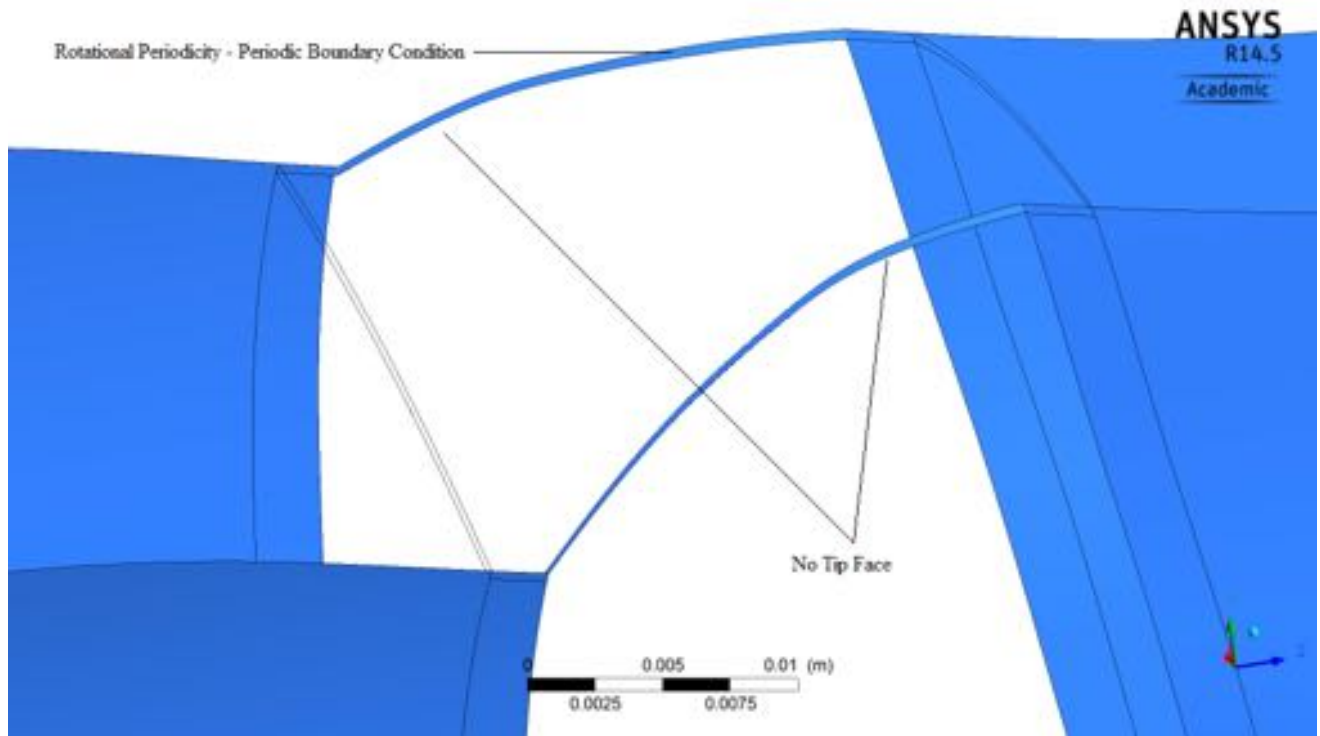


Figure 42 Periodic Boundary condition (Model-III)

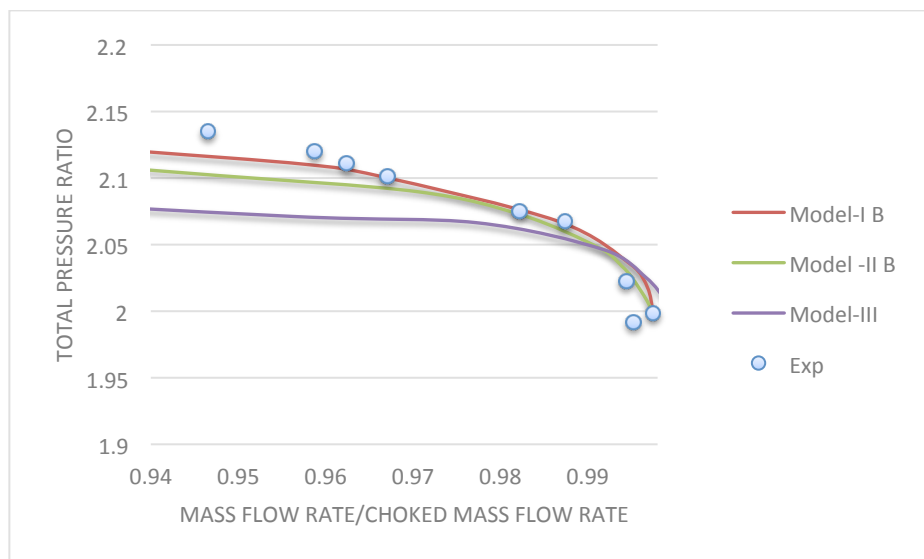


Figure 43 Total pressure ratio Vs. Normalized mass flow rate (Model-I B, II B and III)

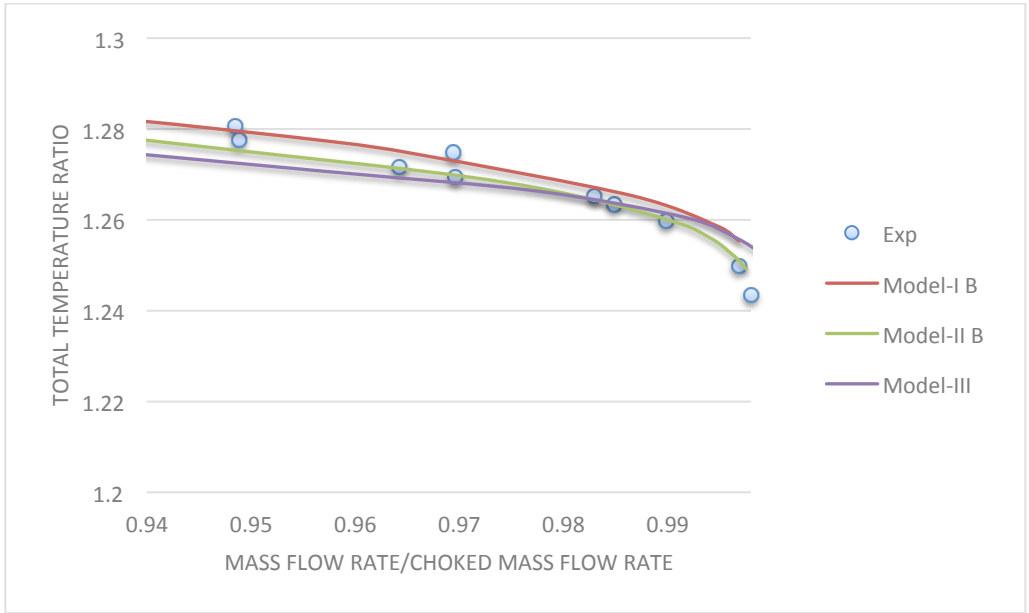


Figure 44 Total temperature ratio Vs. Normalized mass flow rate (Model-I B, II B and III)

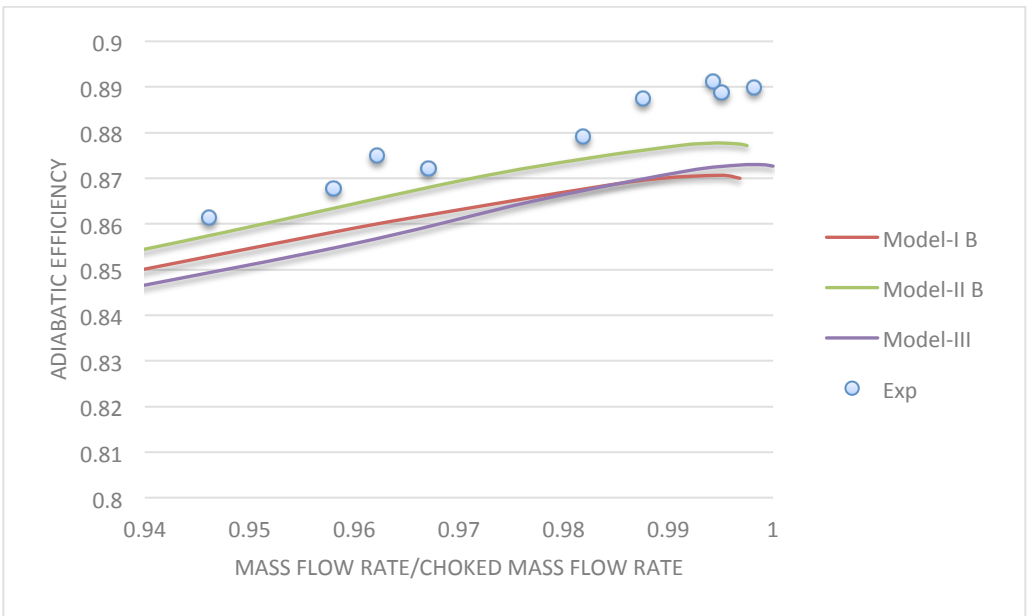


Figure 45 Adiabatic efficiency Vs. Normalized mass flow rate (Model-I B, II B and III)

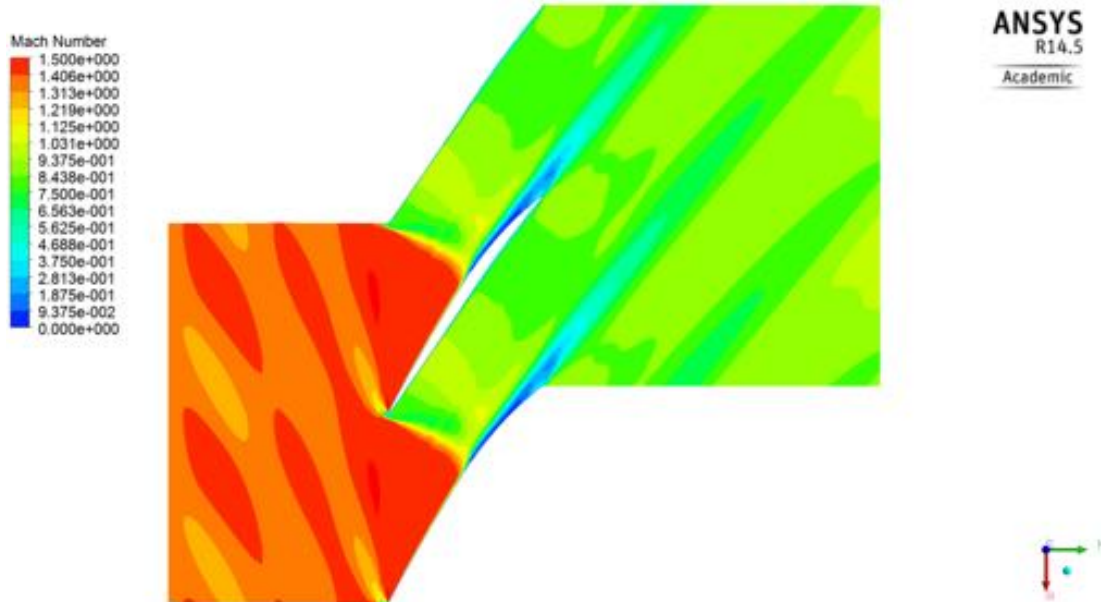


Figure 46 Blade-Blade Mach number contour at 70% span and 98% choked flow (MODEL-III)

The blade-blade Mach number contour for Model-III (see Figure 46) matches well with the experimental result shown in Figure 38. The numerical model predicted the total temperature ratio close to the experimental data (Figure 44) and under predicted the total pressure ratio and adiabatic efficiency (Figures 43 and 45). The predictions are accurate up to 96% of the choked mass flow rate. Since the computed blade-blade Mach number contour comparison was good, this defect could be the result of the tip vortex flow. To analyse the tip vortex effects in detail for the Model-III, four results were generated, two showing the tip vortex of Model-II b at 97% and 95% of choked flow, and two showing the tip vortex of Model-III at 97% and 95% of the choked flow.

The Figure 43 shows the different intensity of tip vortex flow at the different flow conditions. The decrease in the tip vortex intensity is an attribute of stall condition [61]. The tip vortex for a high mass flow condition is tighter and causes a smaller blockage of the flow. From Figure 47, the tip vortex intensity for Model-II B is reduced with the mass flow rate resulting in more

blockage of the flow and therefore increasing the total pressure. The tip vortex intensity did not vary with the mass flow rate in Model-III and therefore less blockage occurs and no increase in total pressure. This is due to the absence of tip clearance flow as there is simply no flow through the tip gap. Tip clearance flow has an important role to play in the performance of the rotor. Therefore Model-III is suitable only for flow conditions between 97%-100% of choked flow.

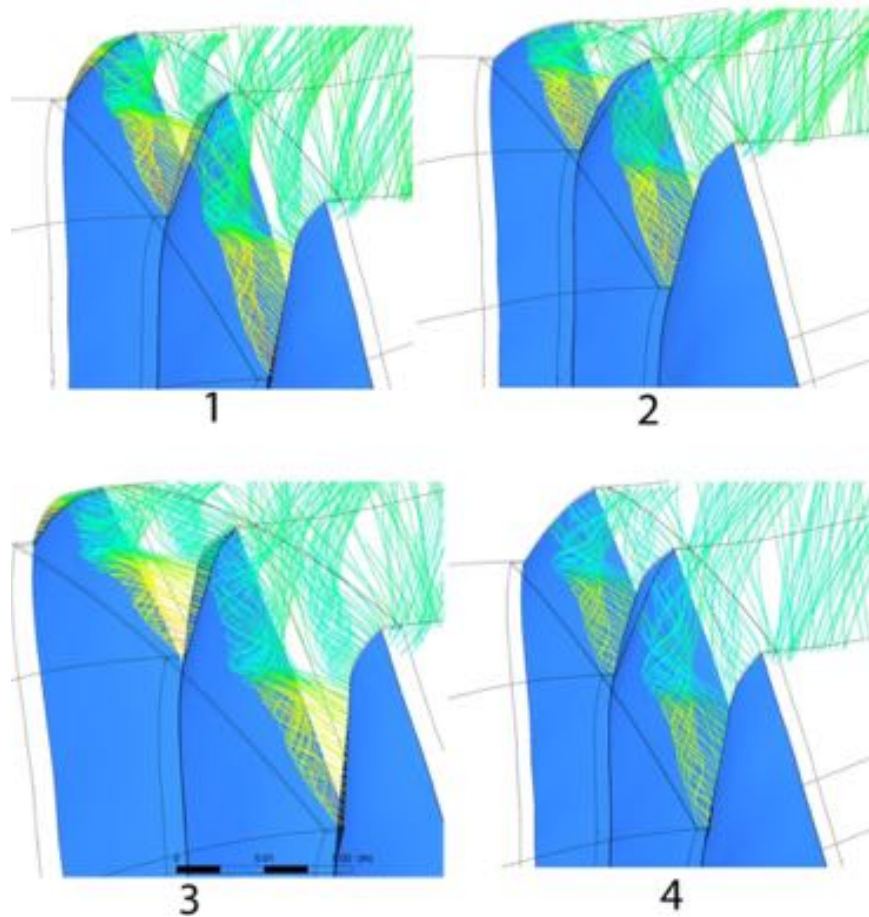


Figure 47 Tip Vortex flow

Case 1. Tip flow in Model-II b at 97% of choked flow. Case 3. Tip flow in Model-II b at 95% of choked flow.

Case 2. Tip flow in Model-III at 97% of choked flow. Case 4. Tip flow in Model-III at 95% of choked flow.

4.2.3 Block-Interface Effects

Further, the Model-II B is used for evaluating the interface modelling. To evaluate the interface methods, four models with different interface connecting techniques, different grid density and

one-one mapped nodes at the interface were modelled. All the four models were solved for 98% choked flow condition. The blade-blade relative Mach numbers from the results are plotted along the pitch at 50% of the span at station 2 and station 3. These stations are located exactly after the block-interface location; therefore comparing the results from a location after the block-interface with the experimental data should be a good way to evaluate the interface methods. Detailed descriptions of the models are tabulated in the Table 7.

Table 7 Computational model description (Model-II D, E, F, G)

MODELS	Model Description	Interface technique	Number of nodes in million
Model-II D	Same as Model-II B, fine grid at the block interfaces, nodes are not mapped one-one.	Frozen Rotor Interface	1.4
Model-II E	Same as Model-II B, fine grid at the block interfaces, nodes are not mapped one-one.	General connection	1.4
Model-II F	Same as Model-II B, medium grid at the block interfaces, nodes are not mapped one-one.	Frozen Rotor Interface	1.18
Model-II G	Same as Model-II B, very fine grid at the block interfaces, nodes are mapped one-one.	Frozen Rotor Interface	1.6

All the four models were solved for 98% choked mass flow rate conditions with the same boundary conditions as in the previous computations. All the models converged for RMS of 10^{-6} and the relative Mach number at 50% span varying with pitch is plotted in Figures 48 and 49. Model-II F took the least computational time but provided the least accuracy. And Model-II D, E and G predicted the experimental curves close enough with Model-II G taking more computational time than other models. The curves plotted between the Model-II D and G shows it's not necessary for the nodes at the interface to be mapped one-one or that the interface needs

to be very refined. Also from the curves between Model-II D and E shows it is not compulsory in this case that the Frozen Rotor Interface method be used in modelling the interface between a block in the stationary hub and a block in the rotating hub.

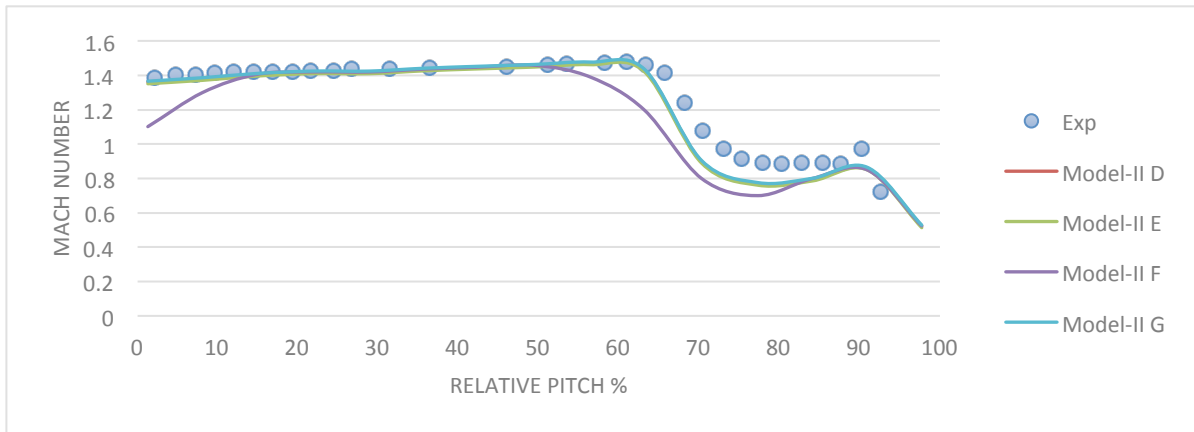


Figure 48 Mach number distribution at Station 2 and span 50% at 98% choked flow

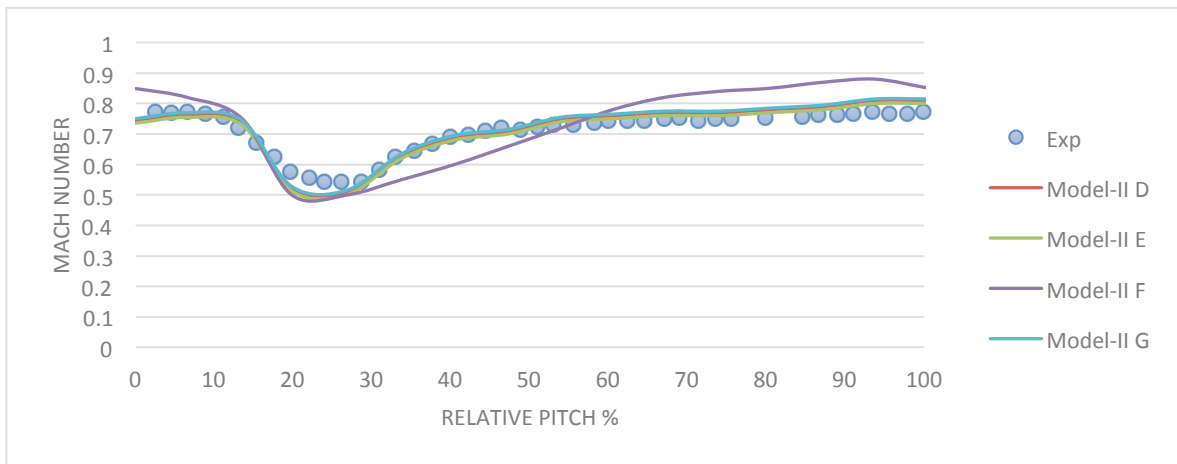


Figure 49 Mach number distribution at Station 3 and span 50% at 98% choked flow

From the Figures 41 and 42 it can be seen that the interfacing methods, except for the medium density grid interface, performs the same. The agreement with the experiment results is good, while all the models slightly under predicted the Mach number after the shock at station 2 and very slightly over predicted the Mach number after the wake at station 3.

4.2.4 Inlet and Outlet Effects

Model-II B was retested for a i) fully-turbulent flow at the inlet and ii) constant total pressure and total temperature value instead of the inlet profile. The computed results for both these cases did not significantly affect the results shown in the previous sections. Additionally, there were no significant variations in the computational time.

Model-II B, when solved for a constant static pressure over the entire outlet (instead of only at the hub) under predicted the mass flow rate and the predicted results along the span did not capture the shape of experimental data.

4.2.5 Conclusion on Performance assessment

After analysing the predictions of the Model-I and Model-II with the experimental data, the modified models (Model-II) predicted the results close to the experimental data. Additionally, Model-II B predicted results near the casing and adiabatic efficiency better than Model-I B.

4.3 Computational Resources assessment

Table 7 shows the computational resources required for the models that closely agreed with the experimental results. The tabulated values are acquired from solving the models under near peak efficiency conditions. Comparing the computational resources required, Model-II B, Model-II E and Model-III use the least time and memory. However Model-III works efficient only for a narrow range of mass flow rates i.e. 100% to 97.5% of choked mass flow rate. Both Model-II B and Model-II E are accurate up to near peak conditions. Based on the mass flow rate condition, available computational resource, and analysis requirements, any of Model-II E or Model-II B or also Model-III can be selected for research works.

Table 8 Computational Resources Assessment

MODEL	Model Description	Number of nodes in millions	Memory required per processor in GB	Computational time per processor in hours
Model-I B	Similar to test case - blade is not split	1.8	0.755	3.81
Model-II B	Blade is split and tip-face attached to one side.	1.4	0.60	2.72
Model-III	Blade is split with no tip face	1.26	0.533	2.38
Model-II D	Frozen Rotor Interface method and fine grids at all the interfaces.	1.4	0.60	2.72
Model-II E	General connection method and fine grids at all the interface	1.4	0.60	2.58
Model-II G	Frozen Rotor Interface method, very fine and one-one mapped grids at all the interfaces.	1.6	0.673	3.13

4.4 Discussions

4.4.1 Performance vs. Computational Resources

Comparing all the models from Figure 43-45, Model-I B performed better in predicting the experimental results near stall conditions and also near operating conditions. Whereas Model-II B predicted the experimental results of adiabatic efficiency much better than Model-IB, but predicted stagnation pressure ratio and stagnation temperature ratio a less well than the Model-I B near the stall conditions. Comparing the radial performance of the models at near operating conditions, all the models failed to capture the hub leakage flow, yet Model-II B predicted the experimental results near the casing better than any other model [Figure 35 and 36]. Comparing the computational resources, Model-II B requires less memory to solve (less by 0.155 GB per

processor) and less computational time (less by an hour) than Model-I B. Whereas Model-III (model with no tip face or tip passage flow) requires even less memory than Model-II B i.e. 0.533GB less per processor, the disadvantage of Model-III is that it is only effective in matching experimental results at high mass flow rate conditions (97%-100% of choked mass flow rate). From the overall analysis, Model-II B with a modified tip passage gives better prediction over a wide range of mass flow rates with the least computational resources. Further the computational time and memory usage can be reduced by using the general connection method at the block interfaces. The frozen rotor had no effect as the entire domain was rotating. Also, the nodes are not necessarily required to be mapped at the inlet block and outlet block interfaces.

4.4.2 Effects of Geometrical Remodelling

The computational domain was modified to reduce the complexity in the geometry. The sharp changes in geometry created skewness and irregular grid elements when the two dimensional grids on the faces were swept to produce the three dimensional grids. By the modification made to the typical computational domain of Rotor 37, each face in the domain had a separate block without any interference from other faces or grid elements. This resulted in grid elements regularly spaced with less skewness and aligned normal to mean flow directions, capturing the flow features effectively. A similar computational grid is possible in Model-I by dividing the flow domain into more number of blocks. Thus by dividing the domain into many blocks, the complexity in the geometry is reduced and many interfaces are formed. The flow inside the blade passage and, tip passage is complex and three dimensional, therefore the node distribution has to be smooth at each interface to reduce the approximation error made during the computation. This ultimately increases the number of nodes and results in additional requirements of computational resources.

5 CONCLUSIONS & RECOMMENDATIONS

Turbomachinery flows exhibit many complex physical phenomena. The best way to improve these predictions is by understanding the physical phenomena and the features of the codes that model them. The aim of the current thesis was to define the role of the computational domain settings (or computational modelling methods) in achieving accurate simulations with the use of least computational resources. This was achieved by creating three main models, they are: Model-I (similar to prior test cases, variants: A, B, C), Model-II (tip face attached to one side of the blade, variants: A, B, C) and Model-III (no tip face).

All the models predicted accurately the shape of the performance curves, but failed to capture the corner stall near the hub due to the hub leakage flow. Except for Model-II B, the others models over predicted the tip-clearance loss and resulted error in the efficiency predictions. The Model-III was efficient only for the high mass flow conditions due to absence of tip clearance flow that resulted in early stall characteristics in Model-III. Both Model-I B and Model-II B were efficient over the mass flow range from choked flow to near stall conditions, but Model-II used lesser memory and converged quicker than Model-I.

Model-II B reduced the required computer memory by 20.5% and computational time by 28.3% of Model-IB (standard method). Model-III reduced the required computer memory by 29.4% and computational time by 37.5% in comparison to the standard method of Model-IB. The operating range of Model-III is very limited and can be used for solving cases only with high mass flow rate conditions. Further change in computational settings applied to Model-II B (i.e. Model-II E) reduced the computational time by 5% of Model-II B. This thesis demonstrates that the computational domains can be remodelled to reduce computational time and memory.

In the current research, the grids were adequately refined to enforce zero wall function. Therefore in future works, the computational domains could be modelled with fewer nodes within the boundary layer and solved with a suitable wall-function technique to possibly further reduce the computational time. Future work should examine the use of these models for transient conditions and study the performances of these models for interactions of the flow with next blade in the row.

REFERENCES

- [1] Gorla, R. S. R., *"Turbomachinery: Design and Theory"*, CRC Press, 2003.1
- [2] Schobeiri, M. T., *"Turbomachinery: Flow Physics and Dynamic Performance"*, Springer, Berlin, 2005.
- [3] Chernobrovkin, A. A., and Lakshminarayana, B., 1999, *"Numerical Simulation of Complex Turbomachinery Flows"*, CR209303, NASA.
- [4] Pratt & Whitney. (n.d.). Retrieved from Pratt & Whitney Web site:
http://www.pw.utc.com/GP7200_Engine
- [5] Xiaodong, W., 2010, *"CFD Simulation of Complex Flows in Turbomachinery and Robust Optimization of Blade Design"*, VUBPRESS, Brussels.
- [6] Ernesto, B., and Biollo, R., 2010, *"Aerodynamics of Swept and Leaned Transonic Compressor-Rotors"*, Department of Mechanical Engineering, University of Padova, Italy.
- [7] Wood, J. R., Strazisar, A. J., and Simonyi, P. S., 1987, *"Shock Structure Measured in a Transonic Fan using Laser Anemometry"*, AGARD CP-401.
- [8] Hirsch, Ch. 2007, *"Numerical Computation of Internal and External Flows"*, Butterworth-Heinemann, Burlington, 2nd edition.
- [9] Herrick, G. P., 2008, "Facilitating higher-fidelity simulation of axial compressor instability and other turbomachinery flow conditions", UMI, Mississippi.

- [10] Ni, R.-H. 1981, "*A Multiple Grid Scheme for Solving the Euler Equations*", Computational Fluid Dynamics Conference, American Institute of Aeronautics and Astronautics, pp. 257-264.
- [11] R. A. Delaney, 1982, "*Time-marching analysis of steady transonic flow in turbomachinery cascades using the hopscotch method*", Tech. Rep. 82-GT-152, American Society of Mechanical Engineers.
- [12] Adamczyk, J. J. 1984, "*Numerical aspects of unsteady flow calculations, in Unsteady Flow in Turbomachines*", vol. 2, Von Karman Institute for Fluid Dynamics.
- [13] Adamczyk, J. J. 1984, "*Model equation for simulating flows in multi-stage turbomachinery*", Tech. Rep. TM-86869, National Aeronautics and Space Administration.
- [14] Hah, C. 1984, "*A Navier-stokes analysis of three-dimensional flows inside turbine blade rows at design and off-design conditions*", ASME Journal of Engineering for Gas Turbines and Power, vol. 106, pp. 421-429.
- [15] Hah, C. 1986, "*A numerical modeling of end-wall and tip-clearance flow of an isolated compressor rotor*", ASME Journal of Engineering for Gas Turbines and Power, vol. 120, pp. 15-21.
- [16] Weinberg B. C., Yang R.-J., McDonald, H. and Shamroth, S. J. 1986, "*Calculations of two and three-dimensional transonic cascade flow fields using the Navier-stokes equations*", ASME Journal of Engineering for Gas Turbines and Power, vol. 108, pp. 93-101.

- [17] Chima, R. V. and Yokota, J. W. 1988, "*Numerical analysis of three-dimensional viscous internal flows*", vol. 1, (Cincinnati, Ohio), pp. 17-24, AIAA, ASME, SIAM, and APS National Fluid Dynamics Congress.
- [18] Janus, J. M. 1989, "*Advanced 3-D CFD Algorithm for Turbomachinery*", PhD thesis, Mississippi State University, Mississippi.
- [19] Fluent 6.3 User's Guide
- [20] AGARD-AR-335, "*CFD Validation for propulsion system components*", 1998. ISBN 92-836-1075-X/ NASA-19980203538.
- [21] Veuillot, J.P. and Meauze, G, 1985, "*A 3D Euler method for internal transonic flow computations with a multi-domain approach*", AGARD-LS-140
- [22] Arnone, A., Liou, M., and Povinelli, L., 1993, "*Multigrid calculations of three-dimensional viscous cascade flows*", J. Propulsion and Power, vol. 9, p.605
- [23] Djayapertapa, L. and Allen, C.B., 2001, "Simulation of transonic flutter and active shockwave control", International Journal of Numerical Methods for Heat & Fluid Flow, Vol. 14 No. 4, 2004, pp. 413-443.
- [24] Chima, R.V., "GRAPE 2-D Grid Generator for Turbomachinery, User's Manual and Documentation", Version, May 2011.
- [25] Calvert, W., Stapleton, A.W., Emmerson, P.R., Buchanan, C.R., and Nott, C.M., 1997, "Evaluation of a 3D viscous code for turbomachinery", ASME Paper 97-GT-78

- [26] Heider, R., Duboue, J.M., Petot, B., Couaillier, V., Liamis, N., and Billonnet, G., 1993, "*Three-dimensional analysis of turbine rotor flow including tip clearance*", ASME Paper 93GT-111
- [27] Fougères, J.M. and Heider, R., 1994, "*Three-dimensional Navier-Stokes prediction of heat transfer with film cooling*", ASME Paper 94-GT-14
- [28] Choi, D., 1993, "*A Navier-Stokes analysis of film cooling in a turbine blade*", AIAA Paper 93-0158
- [29] Kim, J-H., Choi, K-J., Kim, K-Y., 2011, "*Performance evaluation of a transonic axial compressor with circumferential casing grooves*", Proceedings of institution of Mechanical Engineers, Part A: Journal of Power and Energy 2012 226:218,
- [30] Yin, S., Jin, D., Gui, X., and Zhu, F., 2010, "*Application and Comparison of SST Model in Numerical Simulation of the Axial Compressors*", Aero-Engines Simulation Research Centre, Beijing, China.
- [31] Benini, E., Biollo, R., Ponza, R., 2010, "*Efficiency enhancement in transonic compressor rotor blades using synthetic jets: A numerical investigation*", Elsevier Pub, Italy.
- [32] Bassi, F., Rebay, S., and Savini, M., 1991, "*Transonic and supersonic inviscid computations in cascades using adaptive unstructured meshes*", ASME Paper 91-GT-312
- [33] Trepanier, J.Y., Paraschivoiu, M., and Reggio, M., 1993, "*Euler computations of rotor-stator interaction in turbomachinery cascades using adaptive triangular meshes*", AIAA Paper 93-0386

- [34] Kwon, O.J. and Hah, C, 1993, *"Three-dimensional unstructured grid Euler method applied to turbine blades"*, AIAA Paper 93-0196
- [35] Dawes, W.N., 1992, *"The simulation of three-dimensional viscous flow in turbomachinery geometries using a solution adaptive unstructured mesh methodology"*, J. Turbomachinery, vol.114, p.528
- [36] Dawes, W.N., 1993, *"The extension of a solution-adaptive three-dimensional Navier-Stokes solver toward geometries of arbitrary complexity"*, J. Turbomachinery, vol.115, p.283
- [37] Nakahashi, K., Nozaki, O., Kikuchi, K., and Tamura, A., 1987, *"Navier-Stokes computations of two and three-dimensional cascade flow fields"*, AIAA Paper 87-1315
- [38] Mathur, S.R., Madavan, R.N., and Rajagopalan, R.G., 1993, *"A hybrid structured-unstructured method for unsteady turbomachinery flow computations"*, AIAA Paper 93-0387
- [39] Spalart, P.R. and Allmaras, S.R., 1992, *"A one equation turbulence model for aerodynamic flows"*, AIAA Paper 920439
- [40] Spalart, P.R. and Allmaras, S.R., 1994, *"A one-equation turbulence model for aerodynamic flows"*, La Recherche Aerospaciale, 1994 No.1, p. 5
- [41] Jones, W.P. and Launder, B.E., 1973, *"The calculation of low-Reynolds-number phenomena with a two-equation model of turbulence"*, J. Heat and Mass Transfer, vol. 16, p. 1119
- [42] Wilcox, D.C. and Rubesin, M.W., 1980, *"Progress in turbulence modeling for complex flow fields including effects of compressibility"*, NASA Technical Paper 1517

- [43] Wilcox, D.C, 1991, *"Turbulence Modelling for CFD"*, DCW Industries Inc., La Cafiada, California
- [44] Coakley, T.J., 1983, *"Turbulence modeling methods for the compressible Navier-Stokes equations"*, AIAA Paper 83-1693
- [45] Wilcox, D.C, 1994, *"Simulation of transition with a two-equation turbulence model"*, AIAA Jnl, vol.32, no.2, p.247
- [46] Chima, R.V., Giel, P.W. and Boyle, R.J., 1993, *"An algebraic turbulence model for three-dimensional viscous flows"*, in Engineering Turbulence Modelling and Experiments 2, Rodi, W. and Martelli, F. (Eds), Elsevier Pub., N.Y., p.775 [Also NASATM-105931]
- [47] Yi, W., Ji, L., Tian, Y., Shao, W., Li, W. and Xiao, Y., 2010, *"An aerodynamic design and numerical investigation of transonic centrifugal compressor stage"*, Journal of Thermal Science Vol.20, No.3, p.211-217
- [48] Beard, P. F., Smith, A. D. and Povey, T., 2010, *"Experimental and computational fluid dynamics investigation of the efficiency of an unshrouded transonic high pressure turbine"*, Proceedings of institution of Mechanical Engineers, Part A: Journal of Power and Energy 2011 225:1166
- [49] Jennions, I. K. and Turner, M.G., 1993, *"Three-dimensional Navier-Stokes computations of transonic fan flow using an explicit flow solver and an implicit $k - \epsilon$ solver"*, ASME J. Turbomachinery, vol.115, p.261

- [50] Grönman, A., Turunen-Saaresti, T., Royatta, P., Jaatinen, A. and Backman, J., 2012, "*Performance and flow fields of a supersonic axial turbine at off-design conditions*", Proceedings of institution of Mechanical Engineers, Part A: Journal of Power and Energy 2013 227:285
- [51] Geng, S. J., Chen, N.X., Zhang, H.W. and Huang, W.G., 2012, "*An improvement on the efficiency of a single rotor transonic compressor by reducing the shock wave strength on the blade suction surfaces*", Journal of thermal Science Vol.21, No. 2, p127-135
- [52] Cahen, J., Couaillier, V., Delay, J., and Pot, Th., 1993, "*Validation of a Navier-Stokes code using a $k - \epsilon$ turbulence model applied to a three-dimensional transonic channel*", AIAA Paper 93-0293.
- [53] Ciorciari, R., Lesser, A., Blaim, F. and Niehuis, R., 2011, "*Numerical Investigation of tip clearance effects in an axial compressor*", Journal of thermal science Vol.21, No.2 (2012) 109-119.
- [54] Ahn, C-S. and Kim, K-Y., 2003, "*Aerodynamic design optimization of compressor rotor with Navier-Stokes analysis*", Proceedings of institution of Mechanical Engineers, J. ProQuest Science, 217, 2, p.179
- [55] Yang, H., Zheng, Q., Luo, M., Sun, L. and Bhargava, R., 2009, "*Wet Compression performance of a transonic compressor rotor at its near stall point*", J. Marine Sci. Appl. (2011) 10: 49-62
- [56] Reid, L. and Moore, R.D., 1978, "*Design and overall performance of four highly loaded, high-speed inlet stages for an advanced high-pressure-ratio core compressor*", NASA TP 1337

- [57] Moore, R.D. and Reid, L., 1980, *"Performance of single-stage axial flow transonic compressor with rotor and stator aspect ratios of 1.19 and 1.26, respectively, and with design pressure ratio of 2.05"*, NASA TP 1659
- [58] Suder, K. L., Chima, R. V., Strazisar, A. J., and Roberts, W. B., 1995, *"The effect of adding roughness and thickness to a transonic axial compressor rotor"*, ASME J. Turbomachinery, vol.117, no.4, p.491
- [59] Suder, K.L. and Celestina, M.L., 1996, *"Experimental and computational investigation of the tip clearance flow in a transonic axial compressor rotor"*, ASME Paper 94-GT-365 [also ASME J. Turbomachinery, vol.118, no.2, p.218, 1996]
- [60] Hathaway, M.D., Chriss, R.M., Wood, J.R., and Strazisar, A.J., 1993, *"Experimental and computational investigation of the NASA low-speed centrifugal compressor flow field"*, ASME J. Turbomachinery, vol.115, no.3, p.527
- [61] Boretti, A., 2010, *"Experimental and Computational Analysis of Transonic Compressor Rotor"*, 17th Australasian Fluid Mechanics Conference, Auckland
- [62] Shabbir, A., Celestina, M. L., Adamczyk, J.J. and Strazisar, A. J., 1997, *"The Effect of Hub Leakage Flow on Two High Speed Axial Compressor Rotors"*, ASME Paper 97-GT-346
- [63] Chima, Rodrick V., 2009, *"SWIFT Code Assessment for Two Similar Transonic Compressors"*, NASA/TM-2009-215520
- [64] Ameri, Ali A., 2010, *"NASA Rotor 37 Code Validation Glenn-HT Code"*, NASA/CR-2010-216235

[65] Denton, J. D., "Lessons from Rotor 37", 1997, Journal of Thermal Science, Vol. 6, No. 1.